

# Constrained Nonnegative Matrix Factorization for Blind Hyperspectral Unmixing incorporating Endmember Independence

E.M.M.B. Ekanayake<sup>a,\*</sup>, Bhathiya Rathnayake<sup>a</sup>, G.M.R.I. Godaliyadda<sup>b</sup>, H.M.V.R. Herath<sup>b</sup>, M.P.B. Ekanayake<sup>b</sup>

<sup>a</sup>Office of Research and Innovation Services, Sri Lanka Technological Campus, CO 10500, Sri Lanka

<sup>b</sup>Department of Electrical and Electronic Engineering, University of Peradeniya, KY 20400, Sri Lanka

---

## Abstract

Hyperspectral image (HSI) analysis has become a key area in the field of remote sensing as a result of its ability to exploit richer information in the form of multiple spectral bands. The study of hyperspectral unmixing (HU) is important in HSI analysis due to the insufficient spatial resolution of customary imaging spectrometers. The endmembers of an HSI are more likely to be generated by independent sources and be mixed in a macroscopic degree before arriving at the sensor element of the imaging spectrometer as mixed spectra. Over the past few decades, many attempts have focused on imposing auxiliary constraints on the conventional nonnegative matrix factorization (NMF) framework in order to effectively unmix these mixed spectra. Signifying a step forward toward finding an optimum constraint to extract endmembers, this paper presents a novel blind HU algorithm, referred to as Kurtosis-based Smooth Non-negative Matrix Factorization (KbSNMF) which incorporates a novel constraint based on the statistical independence of the probability density functions of endmembers. Imposing this constraint on the conventional NMF framework promotes the extraction of independent endmembers while further enhancing the parts-based representation of data. The proposed algorithm manages to outperform several state of the art NMF-based algorithms in terms of extracting endmembers from hyperspectral remote sensing data, hence could uplift the performance of recent deep learning HU methods which utilizes the endmembers as supervisory input data for abundance extraction.

*Keywords:* Hyperspectral unmixing (HU), blind source separation, kurtosis, constrained, Gaussianity, endmember independence, nonnegative matrix factorization (NMF).

---

## 1. Introduction

A hyperspectral image (HSI) is a multidimensional dataset which consists of large amount of spectral as well as spatial data. Modern-day spectrometers have the ability to capture HSIs with hundreds of narrow spectral bands [1–3]. As a result, HSI technology has become a leading imaging technology in many fields including medical imaging and diagnostics, biotechnology, food quality assessment, forensic sciences and surveillance [4–10]. Advancement in

---

\*Corresponding author

*Email addresses:* mevanekanayake@gmail.com (E.M.M.B. Ekanayake), bhathiyaeng@gmail.com (Bhathiya Rathnayake), roshangodaliyadda777@gmail.com (G.M.R.I. Godaliyadda), vijitha@eng.pdn.ac.lk (H.M.V.R. Herath), mpb.ekanayake@ee.pdn.ac.lk (M.P.B. Ekanayake)

HSI analysis has also affected the field of remote sensing over the past few decades with regard to a multitude of applications like wildlife management, urban planning, surveying, resources management, deforestation monitoring, and agricultural applications [11–13].

However, due to the insufficient spatial resolution of spectrometers utilized for remote sensing applications and homogeneous mixture of distinct macroscopic materials in imaging scenes, the observed reflectance spectrum at each pixel of an HSI could easily be a mixture of several constituent spectra (also called endmembers). This mixing phenomenon constitutes a major concern with regard to many remote sensing tasks such as anomaly detection, mineral mapping, classification and clustering, etc. As a remedy to this complication, various methods of hyperspectral unmixing (HU) have been implemented in order to extract the endmembers from each pixel along with their fractional composition (also called abundances) [14]. The HU problem is in fact a study of three subproblems, *i.e.* determining the no. of endmembers, extracting the endmembers, and realizing their abundances [15]. Thus, given an HSI, the ultimate objective is to find the endmembers along with their abundances at each pixel.

In the past, many algorithms have been introduced in order to solve the HU problem [14, 16–20] and these algorithms can be categorized under two main schemes according to the basic computational approach followed: (1) statistical algorithms and (2) geometric algorithms [21, 22]. Statistical algorithms interpret a mixed pixel by utilizing statistical representations. These representations are commonly analytical expressions based on their underlying probability density functions. Bayesian self organizing maps (BSOM) [23], independent component analysis (ICA) [24, 25], independent factor analysis (IFA) [26], dependent component analysis (DECA) [27], automated morphological endmember extraction (AMEE) [28], and spatial-spectral endmember extraction algorithm (SSEE) [29] are some of the popular statistical algorithms utilized for HU. Geometric algorithms exploit the geometric orientation of HSI data in an  $n$ -dimensional space, where  $n$  is the no. of spectral bands captured by the spectrometer. Vertex component analysis (VCA) [30], minimum volume transform (MVT) [31], simplex identification via split augmented Lagrangian (SISAL) [32], optical real-time adaptive spectral identification system (ORASIS) [33], iterative error analysis (IEA) [34], and nonnegative matrix factorization (NMF) [35] are some of the geometric algorithms frequently utilized to solve the HU problem.

In the recent past, several approaches have been introduced where deep learning (DL) is utilized for HU [2, 36, 37]. With the advancement in artificial intelligence, supervised as well as unsupervised DL based architectures have been introduced. More often, DL based methods for HU do not perform blind unmixing, *i.e.* extract both endmembers and abundances. [38] utilizes a Hopfield neural network (HNN) machine learning approach to solve the seminonnegative matrix factorization problem intended for abundance and nonlinear coefficient estimation, which has illustrated promising performance with regard to abundance extraction when given reliable supervisory endmember data. In [39], an artificial neural network (ANN) is utilized to inverse the pixel spectral mixture in Landsat imagery. Here, to train the network, a spectral library had been created, consisting of endmember spectra collected from the image and simulated mixed spectra. In [40], a neural network (NN) architecture consisting of two stages has been

introduced. The first stage reduces the dimension of the input vector utilizing supervisory endmember data, while the second stage performs the mapping from the reduced input vector to the abundance percentages. As it can be seen, most of the current DL based methods for HU utilize endmembers as supervisory input data in order to extract the abundances.

Originally introduced by Lee and Seung [35], NMF is a mathematical tool which is utilized to decompose a nonnegative data matrix into the product of two other nonnegative matrices of lower rank based on the optimization of a particular objective function. Since the nonnegativity criteria does not accommodate any negative elements in resultant matrices, NMF possess the intuitive notion of combining by parts to form a whole [41], which also coincides with the objective of HU. As a results, NMF based algorithms are often utilized to solve the HU problem more effectively while assuming a linear mixture model (LMM)<sup>1</sup> [21]. However, NMF is an ill-posed geometric algorithm, thereby does not possess a unique solution [42]. The non-convex objective functions utilized for NMF compel its solution space to be wide. Thus, many researchers have introduced novel NMF algorithms by adding different constraints to the conventional NMF algorithm in order to improve the uniqueness of its solution with respect to the HU setting, nonsmooth NMF (*ns*NMF) [43], minimum volume rank deficient NMF (Min-vol NMF) [44], Robust Collaborative NMF (R-CoNMF) [45],  $l_{1/2}$ -sparsity constrained NMF ( $l_{1/2}$ -NMF) [42], spatial group sparsity regularized NMF (SGSNMF) [46], and Graph regularized NMF (GNMF) [47] are some popular NMF algorithms utilized for HU.

In HU, the endmembers are typically constituent spectra corresponding to familiar macroscopic objects in the HSI scene, such as soil, water, vegetation, etc [15]. In a broader sense, HU attempts to find these macroscopic objects by utilizing the observations of signals that have already interacted (or mixed) with other objects in the scene before arriving at the sensing element of the spectrometer. It is pragmatic to assume that the pure spectra are a result of different physical processes, and thereby statistically independent<sup>2</sup> [24]. If a particular methodology promotes maximizing the independence of endmembers, each of the endmembers extracted utilizing that particular method will be more independent than the mixed pixels, hence it would be a progression toward the extraction of constituent spectra. Even though the frequently-associated abundance sum-to-one (ASC) constraint [48] in HU does not accommodate the concept of independent sources, algorithms such as ICA, IFA, and independent innovation analysis (IIA) [49] are popular algorithms utilized in HU which consider the independence of endmembers. Also, several attempts have been taken in order to incorporate the independence of endmembers in NMF based algorithms. The authors of [50] have proposed a novel initialization method based on statistical independence between NMF components. [51] has attempted to initialize NMF with a modified ICA method (modifICA-NMF). [52] has introduced a novel effective method unifying independent vector analysis (IVA) and NMF. Our previous work [53] discusses the suitability of utilizing fundamental notions of kurtosis-based ICA to improve the accuracy of the standard NMF algorithm.

Inspired by the interpretable parts-based representations and simplicity of imposing additional constraints to the

---

<sup>1</sup>See Section 2.1 for more background on *LMM*

<sup>2</sup>Throughout the rest of this paper, we refer the “statistical independence” of endmembers as the “independence” of endmembers.

conventional NMF algorithm and motivated by our previous work [10, 53], this study proposes a novel constraint to the conventional NMF framework named Kurtosis constraint. Incorporating this novel constraint along with an abundance smoothing mechanism, we present a novel blind HU algorithm named Kurtosis-based Smooth Nonnegative Matrix Factorization (KbSNMF) along with its two variations based on the objective function utilized, *i.e.* KbSNMF based on Frobenius norm (KbSNMF-fnorm) and KbSNMF based on divergence (KbSNMF-div). The novelty of the proposed algorithm is the incorporation of a constraint representing the independence of the endmembers, *i.e.* the average kurtosis. The motivation of the proposed work is to promote the independence of endmembers while extracting them in accordance to the parts-based representations of the conventional NMF framework, thereby attempting to extract the most realistic constituent spectra from a given HSI. The contributions of this paper are summarized as follows:

1. Introduction of a novel kurtosis-based constraint which promotes the independence of endmembers and the computation of its gradient w.r.t. the factors of the conventional NMF framework.
2. Establishment of a novel blind HU algorithm named KbSNMF, which effectively promotes the independence of endmembers while maintaining the smoothness of abundance maps.
3. Implementation and performance evaluation of the proposed algorithm in comparison with the other state-of-the-art NMF-based blind HU algorithms.

The performance of the proposed KbSNMF algorithm is evaluated through a series of experiments executed on simulated as well as real HSI datasets. These experiments substantiate that the proposed algorithm outperforms several other algorithms which are commonly utilized in HU.

The rest of the paper is arranged as follows. Section 2 provides the background related to the proposed kurtosis-based algorithm. In Section 3, the novel kurtosis-based constraint is developed along with its derivatives. In Section 4, the novel KbSNMF algorithm is presented. Section 5 discusses some key issues related to the implementation of the proposed algorithm. Section 6 is devoted for experimental results and the paper is concluded in Section 7.

## 2. Background

### 2.1. Linear Mixture Model (LMM)

LMM is the most frequently utilized model for HU and its implications had been widely discussed in many previous works [42, 45, 46]. This model highly depends on the assumption that the incident light waves on the HSI scene reflect only once from the underlying macroscopic objects and are captured by the sensing element of the spectrometer without being subjected to scattering. In the LMM, the spectrum at each pixel is represented as a linear combination of the endmember spectra as below,

$$\mathbf{x}_j = \sum_{i=1}^r S_{ij} \mathbf{a}_i + \mathbf{e}_j \quad (1)$$

where  $\mathbf{x}_j \in \mathbb{R}_+^{n \times 1}$  is the  $j^{\text{th}}$  pixel spectrum,  $S_{ij}$  is the abundance fraction of the  $i^{\text{th}}$  endmember and  $j^{\text{th}}$  pixel,  $\mathbf{a}_i \in \mathbb{R}_+^{n \times 1}$  is the spectra of the  $i^{\text{th}}$  endmember of the HSI,  $\mathbf{e}_j \in \mathbb{R}_+^{n \times 1}$  is an additive Gaussian noise associated with modeling errors, and  $r$  is the no. of endmembers in the HSI. All spectra are measured in reflectance values, hence the nonnegativity in  $\mathbf{x}_j$ 's and  $\mathbf{a}_i$ 's. The abundance  $S_{ij}$  is explained as the fractional composition occupied by the  $i^{\text{th}}$  endmember in the  $j^{\text{th}}$  pixel. The nonnegativity constraint  $S_{ij} \geq 0$  and the sum-to-one constraint  $\sum_{i=1}^r S_{ij} = 1$  are implied in order to guarantee that the fractional compositions representing the constituent endmembers are nonnegative and the abundance summation at each mixed pixel equals 1. The LMM can be reformulated in matrix notations as below,

$$\mathbf{X} = \mathbf{A} \times \mathbf{S} + \mathbf{E} \quad (2)$$

where  $\mathbf{X} \in \mathbb{R}_+^{n \times m}$  is the HSI data matrix,  $n$  being the no. of spectral bands and  $m$  being the no. of pixels,  $\mathbf{A} \in \mathbb{R}_+^{n \times r}$  is the endmember matrix whose columns represent the spectra of each of the  $r$  endmembers,  $\mathbf{S} \in \mathbb{R}_+^{r \times m}$  is the abundance matrix whose columns represent the fractional compositions at each of the  $m$  pixels, and  $\mathbf{E} \in \mathbb{R}_+^{n \times m}$  is the noise matrix. This formulation casts the HU problem as a BSS problem, *i.e.* simultaneously extracts the endmembers and their abundances at each pixel while utilizing the HSI as the only<sup>3</sup> input.

## 2.2. Nonnegative Matrix Factorization (NMF)

NMF is a low-rank approximation of nonnegative matrices widely utilized in the fields of computer vision, clustering, data compression, etc [50, 54–56]. NMF was first introduced by Lee and Seung as a parts-based representation technique which permits the data in a nonnegative matrix to be decomposed into two other nonnegative matrices. Given a matrix  $\mathbf{V} \in \mathbb{R}_+^{n \times m}$ , NMF tries to find nonnegative matrices  $\mathbf{W} \in \mathbb{R}_+^{n \times r}$  (known as the source matrix) and  $\mathbf{H} \in \mathbb{R}_+^{r \times m}$  (known as the mixing matrix) which satisfy the approximation below.

$$\mathbf{V} \approx \mathbf{WH} \quad (3)$$

However, there are infinite no. of  $\mathbf{W}$ ,  $\mathbf{H}$  solution pairs which satisfy the above approximation. For instance, it is possible to write  $\mathbf{WH} = (\mathbf{W}\mathbf{\Gamma}^{-1})(\mathbf{\Gamma}\mathbf{H})$  for any invertible  $\mathbf{\Gamma} \in \mathbb{R}_+^{r \times r}$ . The conventional procedure to achieve (3) is by defining an objective function which quantifies the quality of the approximation between the two nonnegative matrices  $\mathbf{V}$  and  $\mathbf{WH}$  and implementing an optimization algorithm to minimize the defined objective function w.r.t.  $\mathbf{W}$  and  $\mathbf{H}$ . One of the most commonly utilized objective function is the square of the frobenius norm between  $\mathbf{V}$  and  $\mathbf{WH}$  as in (4), which is optimal for Gaussian distributed noise [57].

---

<sup>3</sup>Utilizing the LMM as a BSS problem, the no. of endmembers,  $r$  is also seen as an input. However, many previous work have discussed finding the optimum  $r$  for a given HSI dataset, which will be discussed later in this paper. See Section 6.4

$$\|\mathbf{V} - \mathbf{WH}\|_F^2 = \sum_{ij} (V_{ij} - (WH)_{ij})^2 \quad (4)$$

The above expression is lower bounded by zero and distinctly vanishes if and only if  $\mathbf{V} = \mathbf{WH}$ . Another popular objective function is the divergence<sup>4</sup> of  $\mathbf{V}$  from  $\mathbf{WH}$  as in (5), which is optimal for Poisson distributed noise [57].

$$D(\mathbf{V} \parallel \mathbf{WH}) = \sum_{ij} \left( V_{ij} \log \frac{V_{ij}}{(WH)_{ij}} - V_{ij} + (WH)_{ij} \right) \quad (5)$$

Similar to the frobenius norm, the divergence is also lower bounded by zero and vanishes if and only if  $\mathbf{V} = \mathbf{WH}$ . Even though the (4) and (5) functions are convex in  $\mathbf{W}$  and  $\mathbf{H}$  alone, they are not convex in  $\mathbf{W}$  and  $\mathbf{H}$  together [35]. Hence, it is not possible to analytically find global minima of these functions w.r.t.  $\mathbf{W}$  and  $\mathbf{H}$ . However, it is possible to find local minima utilizing numerical optimization methods. Lee and Seung have proposed the below multiplicative update rules (6) and (7) to find local minima of the above (4) and (5) functions respectively.

$$\mathbf{W} \leftarrow \mathbf{W} \circ \frac{\mathbf{VH}^T}{\mathbf{WHH}^T}, \quad \mathbf{H} \leftarrow \mathbf{H} \circ \frac{\mathbf{W}^T \mathbf{V}}{\mathbf{W}^T \mathbf{WH}} \quad (6)$$

$$\mathbf{W} \leftarrow \mathbf{W} \circ \frac{\mathbf{V} \mathbf{H}^T}{\mathbf{1}_{n \times m} \mathbf{H}^T}, \quad \mathbf{H} \leftarrow \mathbf{H} \circ \frac{\mathbf{W}^T \mathbf{V}}{\mathbf{W}^T \mathbf{1}_{n \times m}} \quad (7)$$

Lee and Seung have further proven the convergence of both the above update rules utilizing an auxiliary function analogous to that utilized for proving convergence of the Expectation Maximization algorithm [35].

The LMM model transforms the HU problem into the form of a conventional NMF problem. If  $\mathbf{V}$  is the HSI data matrix  $\mathbf{X}$ , then source matrix  $\mathbf{W}$  is the endmember matrix  $\mathbf{A}$  and mixing matrix  $\mathbf{H}$  is the abundance matrix  $\mathbf{S}$ . Thus given  $\mathbf{X}$ , solving the blind HU problem for  $\mathbf{A}$  and  $\mathbf{S}$  utilizing the conventional NMF problem can be formulated as in (8) and (9) for the frobenius norm based objective function and the divergence based objective function respectively.

$$\arg \min_{\mathbf{A}, \mathbf{S}} \|\mathbf{X} - \mathbf{AS}\|_F^2, \quad \text{s.t. } \mathbf{A}, \mathbf{S} \succeq 0 \quad (8)$$

$$\arg \min_{\mathbf{A}, \mathbf{S}} D(\mathbf{X} \parallel \mathbf{AS}), \quad \text{s.t. } \mathbf{A}, \mathbf{S} \succeq 0 \quad (9)$$

Due to the lack of a unique solution, in order to solve above problems while improving the uniqueness, many researchers have incorporated additional auxiliary constraints on  $\mathbf{A}$  and  $\mathbf{S}$  [42, 44–47].

### 3. Average Kurtosis Constraint

#### 3.1. Kurtosis of a Signal

Central moments are often utilized in signal processing in order to characterize the spread of the probability density function (pdf) of a signal [24]. A normalized version of the forth central moment, given by (10), is called the kurtosis

---

<sup>4</sup>Unlike the frobenius norm, the divergence cannot be designated as a “distance” since it is not symmetric in  $\mathbf{V}$  and  $\mathbf{WH}$ . Thus, it is the common practice to refer to it as the “divergence of  $\mathbf{V}$  from  $\mathbf{WH}$ ”

of a signal. Here  $y$  denotes the signal,  $\bar{y}$  denotes the mean of the signal, and  $\mathbb{E}$  is the expectation operator. Essentially, It provides a measure of the “peaky”ness of the shape of the pdf. Excess kurtosis is a measure which compares the kurtosis of a given pdf with the kurtosis of a Gaussian distribution. Since the kurtosis of a Gaussian distribution equals 3, the excess kurtosis can be defined as in (11).

$$\text{Kurtosis} = \frac{\mathbb{E}[(y - \bar{y})^4]}{(\mathbb{E}[(y - \bar{y})^2])^2} \quad (10)$$

$$\text{Excess kurtosis} = \text{Kurtosis} - 3 \quad (11)$$

Based on the value of excess kurtosis, distributions are categorized under three main types. *Mesokurtic* distribution is close to a Gaussian distribution; has an excess kurtosis closer to zero. *Leptokurtic* (also known as super-Gaussian) distribution has a higher and sharper central peak; tails are longer and flatter; has positive excess kurtosis. *Platykurtic* (also known as sub-Gaussian) distribution has a lower and broader central peak; tails are shorter and thinner; has negative excess kurtosis.

Central Limit Theorem (CLT) [24] ensures that a mixture of signals is approximately Gaussian irrespective of the distributions of the underlying source signals. Even though the converse of CLT is not assured, *i.e.* it is not certain that any Gaussian signal is a mixture of non-Gaussian signals, in practical scenarios, Gaussian signals do consist of a mixture of non-Gaussian signals. Thus, to extract the underlying source signals from a signal mixture, it is a common practice in BSS to define a measure of non-Gaussianity and implement an algorithm which maximizes the defined measure. Subsequently, excess kurtosis seems to be a suitable candidate for this purpose as it is a measure of non-Gaussianity. If the excess kurtosis value of a signal is close to zero, it tempts to be Gaussian and if the excess kurtosis value of a signal is away from zero, it tempts to be non-Gaussian (super-Gaussian or sub-Gaussian). Since, there are two types of non-Gaussian distributions, it is the common practice in most BSS methods to assume that source signals are of only one type. In this work, we assume the constituent spectra of an HSI to have super-Gaussian distributions. Hence, from a given HSI data matrix  $\mathbf{X}$ , we aim to extract an endmember matrix  $\mathbf{A}$ , whose columnwise average kurtosis is maximized, utilizing an NMF framework. Thus we introduce a novel constrained NMF algorithm which incorporates the maximization of the average kurtosis of endmembers.

### 3.2. Average Kurtosis

Obeying the notation introduced in Section 2.1,  $\mathbf{A} \in \mathbb{R}_+^{n \times r}$  is the endmember matrix whose columns represent the spectra of each of the  $r$  endmembers of the HSI. Thus, it is possible to extract the  $i^{\text{th}}$  endmember utilizing a simple matrix manipulation as below,

$$\mathbf{a}_i = \mathbf{A}\Phi_i \quad (12)$$

where  $\mathbf{a}_i$  is spectrum of the  $i^{\text{th}}$  endmember from matrix  $\mathbf{A}$  (or the  $i^{\text{th}}$  column of matrix  $\mathbf{A}$ ) and  $\Phi_i \in \mathbb{R}^{r \times 1}$  is a column vector whose all elements are zeros except for the  $i^{\text{th}}$  element which equals 1. If the kurtosis of the  $i^{\text{th}}$  endmember is

$K_i$ , it can be expressed as below.

$$K_i = \frac{\mathbb{E}[(\mathbf{a}_i - \bar{\mathbf{a}}_i)^4]}{(\mathbb{E}[(\mathbf{a}_i - \bar{\mathbf{a}}_i)^2])^2} \quad (13)$$

Thus the average kurtosis through all  $r$  endmembers,  $\bar{K}$  can be expressed as below utilizing (12) and (13).

$$\begin{aligned} \bar{K} &= \frac{1}{r} \sum_{q=1}^r K_q \\ &= \frac{1}{r} \sum_{q=1}^r \frac{\mathbb{E}[(\mathbf{A}\Phi_q - \overline{\mathbf{A}\Phi_q})^4]}{(\mathbb{E}[(\mathbf{A}\Phi_q - \overline{\mathbf{A}\Phi_q})^2])^2} \end{aligned} \quad (14)$$

Thus  $\bar{K}$  can be written as a function of  $\mathbf{A}$ ,  $\bar{K}(\mathbf{A})$ . We try to maximize  $\bar{K}$  so that the extracted endmembers will have a higher kurtosis, thereby be closer to super-Gaussian signals. Hence, the proposed framework would favorably influence the extraction of constituent spectra of the underlying HSI.

### 3.3. Derivative of Average Kurtosis

In order to incorporate the  $\bar{K}$  constraint on the conventional NMF framework, it is essential to find the gradient or the partial derivative of  $\bar{K}$  w.r.t  $\mathbf{A}$  and  $\mathbf{S}$ , *i.e.*  $\nabla_{\mathbf{A}}\bar{K} \in \mathbb{R}^{n \times r}$  and  $\nabla_{\mathbf{S}}\bar{K} \in \mathbb{R}^{r \times m}$ . Since  $\bar{K}$  is not a function of  $\mathbf{S}$ ,  $\nabla_{\mathbf{S}}\bar{K} = \mathbf{0} \in \mathbb{R}^{r \times m}$ . In this section, we provide a detailed explanation on finding  $\nabla_{\mathbf{A}}\bar{K}$ . Since  $\mathbf{A}$  is the endmember matrix, we denote each of its elements by the notation  $A_{ki}$ , with the meaning of the reflectance value belonging to the  $k^{\text{th}}$  spectral band of the  $i^{\text{th}}$  endmember. Thus the  $(k, i)^{\text{th}}$  element of  $\nabla_{\mathbf{A}}\bar{K}$  can be written as below implementing an element-wise derivative.

$$\begin{aligned} \nabla_{\mathbf{A}}\bar{K}_{ki} &= \frac{\partial \bar{K}}{\partial A_{ki}} \\ &= \frac{1}{r} \sum_{q=1}^r \frac{\partial K_q}{\partial A_{ki}} \end{aligned} \quad (15)$$

For the convenience of simplifying we assume that each of the endmember spectra vectors have unit variance, *i.e.*  $(\mathbb{E}[(\mathbf{a}_i - \bar{\mathbf{a}}_i)^2])^2 = 1, \forall i$ . In order to rectify the effects of this assumption, a normalization is carried out as discussed in Section 5.2.

Since

$$\frac{\partial K_q}{\partial A_{ki}} = \begin{cases} \frac{\partial K_i}{\partial A_{ki}}, & \text{if } q = i \\ 0. & \text{otherwise} \end{cases} \quad (16)$$

and as a result of this assumption, we obtain a simplified version of the partial derivative term  $\nabla_{\mathbf{A}}\bar{K}_{ki}$  as below,



$$\begin{aligned}\nabla_{\mathbf{A}} \overline{K}_{ki} &= \frac{1}{r} \frac{\partial [\mathbb{E}[(\mathbf{a}_i - \overline{\mathbf{a}}_i)^4]]}{\partial A_{ki}} \\ &= \frac{1}{nr} \sum_{p=1}^n \frac{\partial (A_{pi} - \mu_i)^4}{\partial A_{ki}}\end{aligned}\quad (17)$$

where  $A_{pi}$  is the reflectance value belonging to the  $p^{\text{th}}$  spectral band of the  $i^{\text{th}}$  endmember and  $\mu_i$  is the mean reflectance of the  $i^{\text{th}}$  endmember. As it can be seen, the partial derivative term  $\nabla_{\mathbf{A}} \overline{K}_{ki}$  is a summation of  $n$  more partial derivative terms. The following solutions can be easily obtained by utilizing the chain rule in calculus.

$$\frac{\partial}{\partial a_{ki}} (A_{pi} - \mu_i)^4 = \begin{cases} -4(A_{ki} - \mu_i)^3 \left(\frac{1}{n} - 1\right), & \text{if } p = k \\ -4(A_{pi} - \mu_i)^3 \left(\frac{1}{n}\right). & \text{otherwise} \end{cases}\quad (18)$$

Thus, the partial derivative term  $\nabla_{\mathbf{A}} \overline{K}_{ki}$  in (18) can be written as follows.

$$\nabla_{\mathbf{A}} \overline{K}_{ki} = \frac{-4}{nr} [S_i - (A_{ki} - \mu_i)^3]\quad (19)$$

where  $S_i = \frac{1}{n} \sum_{p=1}^n (A_{pi} - \mu_i)^3$  represents a normalized version of the third central moment (skewness) of the  $i^{\text{th}}$  endmember. However, in this work we do not explore the implication of skewness within derivative of the average kurtosis.

Concatenating the element-wise results, we then express  $\nabla_{\mathbf{A}} \overline{\mathbf{K}}$  as the difference between two matrices as below,

$$\nabla_{\mathbf{A}} \overline{\mathbf{K}} = \frac{-4}{nr} (\mathbf{P} - \mathbf{Q})\quad (20)$$

where  $P_{ki} = S_i$  and  $Q_{ki} = (A_{ki} - \mu_i)^3$ . Then,  $\mathbf{Q}$  and  $\mathbf{P}$  can be written as in (21) and (22) respectively for the convenience of incorporating  $\nabla_{\mathbf{A}} \overline{\mathbf{K}}$  in the NMF framework.

$$\mathbf{Q} = \left[ \mathbf{A} - \frac{1}{n} \mathbf{1}_{n \times n} \mathbf{A} \right]^{\circ 3} = [\mathbf{N}\mathbf{A}]^{\circ 3}\quad (21)$$

$$\mathbf{P} = \mathbf{P} = \frac{1}{n} \mathbf{1}_{n \times n} \mathbf{Q} = \frac{1}{n} \mathbf{1}_{n \times n} [\mathbf{N}\mathbf{A}]^{\circ 3}\quad (22)$$

where  $\mathbf{N} = (\mathbf{I} - \frac{1}{n} \mathbf{1}_{n \times n})$  and  $\mathbf{1} \in \mathbb{R}^{n \times n}$  denotes a matrix whose all elements are ones.  $[\cdot]^{\circ 3}$  denotes the Hadamard (element-by-element) power by 3. Finally, from (20),  $\nabla_{\mathbf{A}} \overline{\mathbf{K}}$  can be written as follows.

$$\begin{aligned}\nabla_{\mathbf{A}} \overline{\mathbf{K}} &= \frac{-4}{nr} \left[ \frac{1}{n} \mathbf{1}_{n \times n} [\mathbf{N}\mathbf{A}]^{\circ 3} - [\mathbf{N}\mathbf{A}]^{\circ 3} \right] \\ &= \frac{4}{nr} \left[ \mathbf{N} [\mathbf{N}\mathbf{A}]^{\circ 3} \right]\end{aligned}\quad (23)$$

#### 4. Kurtosis-based Smooth Nonnegative Matrix Factorization (KbSNMF)

In this section, we propose a novel blind HU algorithm which not only promotes the independence of endmembers via the kurtosis constraint, but also promotes the smoothness of the abundance maps by integrating a smoothing matrix to the conventional NMF framework. Hence, we denominate the proposed algorithm as Kurtosis-based Smooth NMF (KbSNMF). In the proceeding sections, we discuss two variations of KbSNMF depending on the function utilized for approximation.

##### 4.1. KbSNMF-fnorm

Here we present KbSNMF based on frobenius norm (KbSNMF-fnorm). The general optimization problem for KbSNMF-fnorm is as below.

$$\arg \min_{\mathbf{A}, \mathbf{S}} \{ \|\mathbf{X} - \mathbf{A}\mathbf{S}\|_F^2 - \gamma \overline{K}(\mathbf{A}) \}, \quad s.t. \mathbf{A}, \mathbf{S} \succeq 0 \quad (24)$$

Here,  $\gamma \in \mathbb{R}_+$  is a parameter which establishes the trade-off between approximation error and non-Gaussianity of the endmembers rendered by  $\overline{K}$  and  $\mathbf{M} \in \mathbb{R}_+^{k \times k}$  is a symmetric matrix called the smoothing matrix which is defined below,

$$\mathbf{M} = (1 - \theta)\mathbf{I} + \frac{\theta}{k} \mathbf{1}_{k \times 1} \mathbf{1}_{k \times 1}^T \quad (25)$$

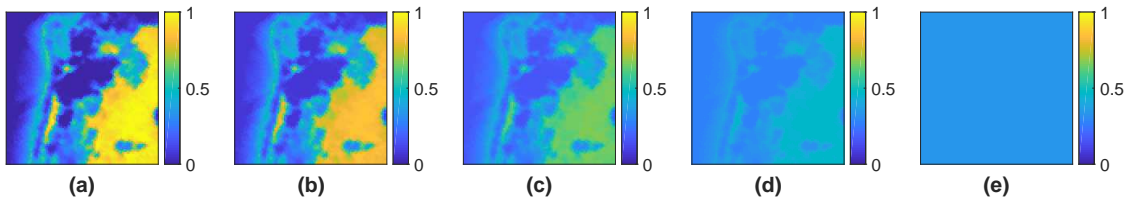


Figure 1: Effects of the smoothing parameter demonstrated on a ground truth abundance map (“soil”) of a real HSI dataset (“Samson”): (a)  $\theta = 0$  (no smoothing), (b)  $\theta = 0.2$ , (c)  $\theta = 0.5$ , (d)  $\theta = 0.8$ , (e)  $\theta = 1$  (maximum smoothing).

In order to find a solution for (24), we consider the objective function below.

$$L_1(\mathbf{A}, \mathbf{S}) = \|\mathbf{X} - \mathbf{A}\mathbf{S}\|_F^2 - \gamma K_{avg}(\mathbf{A}) \quad (26)$$

In order to make the algorithm much simpler, the variable matrices  $\mathbf{A}$  and  $\mathbf{S}$  are updated in turns. In each iteration, first  $\mathbf{A}$  is updated while  $\mathbf{S}$  is kept constant, then,  $\mathbf{S}$  is updated while  $\mathbf{A}$  is kept constant. This scheme is called a block-coordinate descent approach and is widely utilized in NMF based algorithms [58]. The updates rules can be primarily written as follows.

$$\begin{aligned}\mathbf{A} &\leftarrow \mathbf{A} - \eta_{\mathbf{A}} \circ \nabla_{\mathbf{A}} L_1(\mathbf{A}, \mathbf{S}) \\ \mathbf{S} &\leftarrow \mathbf{S} - \eta_{\mathbf{S}} \circ \nabla_{\mathbf{S}} L_1(\mathbf{A}, \mathbf{S})\end{aligned}\quad (27)$$

where  $\circ$  denotes the Hadamard (element-by-element) product. Updating  $\mathbf{A}$  and  $\mathbf{S}$  directly accounts to computing the partial derivatives  $\nabla_{\mathbf{A}} L_1 \in \mathbb{R}_+^{n \times r}$  and  $\nabla_{\mathbf{S}} L_1 \in \mathbb{R}_+^{r \times m}$ , and finding suitable learning rates  $\eta_{\mathbf{A}} \in \mathbb{R}_+^{n \times r}$  and  $\eta_{\mathbf{S}} \in \mathbb{R}_+^{r \times m}$ .

Computing the partial derivatives of  $L_1$  by  $\mathbf{A}$  and  $\mathbf{S}$  can be seen as two parts, *i.e.* partial derivatives of  $\|\mathbf{X} - \mathbf{A}\mathbf{M}\mathbf{S}\|_F^2$  term and  $\gamma \overline{K}(\mathbf{A})$  term. We refer the readers to [43] and [58] for detailed explanation of the partial derivative of  $\|\mathbf{X} - \mathbf{A}\mathbf{M}\mathbf{S}\|_F^2$ . Incorporating the result in (23), we can present the partial derivatives of  $L_1$  as follows.

$$\begin{aligned}\frac{\partial L_1}{\partial \mathbf{A}} &= -2\mathbf{X}\mathbf{S}^T\mathbf{M}^T + 2\mathbf{A}\mathbf{M}\mathbf{S}\mathbf{S}^T\mathbf{M}^T + 2\gamma'\mathbf{N}[\mathbf{N}\mathbf{A}]^{\circ 3} \\ \frac{\partial L_1}{\partial \mathbf{S}} &= -2\mathbf{M}^T\mathbf{A}^T\mathbf{X} + 2\mathbf{M}^T\mathbf{A}^T\mathbf{A}\mathbf{M}\mathbf{S}\end{aligned}\quad (28)$$

where  $\mathbf{I}$  denotes the identity matrix and  $\gamma'$  is scalar quantity which equals  $\frac{-2\gamma}{nr}$ . By substituting these partial derivative terms  $\frac{\partial L_1}{\partial \mathbf{A}}$  and  $\frac{\partial L_1}{\partial \mathbf{S}}$  in the original block-coordinate descent equations in (27), we can obtain the following update rules for KbSNMF-fnorm.

$$\begin{aligned}\mathbf{A} &\leftarrow \mathbf{A} - \eta_{\mathbf{A}} \circ (-2\mathbf{X}\mathbf{S}^T\mathbf{M}^T + 2\mathbf{A}\mathbf{M}\mathbf{S}\mathbf{S}^T\mathbf{M}^T + 2\gamma'\mathbf{N}[\mathbf{N}\mathbf{A}]^{\circ 3}) \\ \mathbf{S} &\leftarrow \mathbf{S} - \eta_{\mathbf{S}} \circ (-2\mathbf{M}^T\mathbf{A}^T\mathbf{X} + 2\mathbf{M}^T\mathbf{A}^T\mathbf{A}\mathbf{M}\mathbf{S})\end{aligned}\quad (29)$$

However, due to the subtracting terms in the gradients, the update rules (29) can enforce  $\mathbf{A}$  and  $\mathbf{S}$  to contain negative elements, which contradicts with the parts based representation of the NMF framework. Thus, following a methodology similar to that proposed by Lee and Seung, we define data-adaptive learning rates  $\eta_{\mathbf{A}}$  and  $\eta_{\mathbf{S}}$  as below in order to ensure all positive elements in  $\mathbf{A}$  and  $\mathbf{S}$  at each update step.

$$\eta_{\mathbf{A}} = \frac{\mathbf{A}}{2\mathbf{A}\mathbf{M}\mathbf{S}\mathbf{S}^T\mathbf{M}^T + 2\gamma'\mathbf{N}[\mathbf{N}\mathbf{A}]^{\circ 3}}, \quad \eta_{\mathbf{S}} = \frac{\mathbf{S}}{2\mathbf{M}^T\mathbf{A}^T\mathbf{A}\mathbf{M}\mathbf{S}}\quad (30)$$

The fraction line denotes element-by-element division. This results in the multiplicative update rules for the proposed KbSNMF-fnorm algorithm as below.

$$\mathbf{A} \leftarrow \mathbf{A} \circ \frac{\mathbf{X}\mathbf{S}^T\mathbf{M}^T}{\mathbf{A}\mathbf{M}\mathbf{S}\mathbf{S}^T\mathbf{M}^T + \gamma'\mathbf{N}[\mathbf{N}\mathbf{A}]^{\circ 3}}, \quad \mathbf{S} \leftarrow \mathbf{S} \circ \frac{\mathbf{M}^T\mathbf{A}^T\mathbf{X}}{\mathbf{M}^T\mathbf{A}^T\mathbf{A}\mathbf{M}\mathbf{S}}\quad (31)$$

For convenience, we can reconfigure the order of matrices and the final update rules for the proposed KbSNMF-fnorm algorithm would be as follows.

$$\mathbf{A} \leftarrow \mathbf{A} \circ \frac{\mathbf{X}(\mathbf{MS})^T}{\mathbf{A}(\mathbf{MS})(\mathbf{MS})^T + \gamma' \mathbf{N}[\mathbf{NA}]^{\circ 3}}, \quad \mathbf{S} \leftarrow \mathbf{S} \circ \frac{(\mathbf{AM})^T \mathbf{X}}{(\mathbf{AM})^T (\mathbf{AM}) \mathbf{S}} \quad (32)$$

It can be seen that choosing the data-adaptive learning rates in the form of (30) to avoid subtraction has enforced  $\mathbf{A}$  and  $\mathbf{S}$  to contain nonnegative elements throughout the block-coordinate descent approach, given initial nonnegative  $\mathbf{A}$  and  $\mathbf{S}$ .

#### 4.2. KbSNMF-div

Analogously, we present the following optimization problem for KbSNMF based on divergence (KbSNMF-div).

$$\arg \min_{\mathbf{A}, \mathbf{S}} \{D(\mathbf{X} \parallel \mathbf{AMS}) - \gamma K_{avg}(\mathbf{A})\}, \quad s.t. \mathbf{A}, \mathbf{S} \succeq 0 \quad (33)$$

Following a similar procedure as in Section 4.1, the following multiplicative update rules can be derived for KbSNMF-div algorithm,

$$\mathbf{A} \leftarrow \mathbf{A} \circ \frac{\frac{\mathbf{X}}{\mathbf{A}(\mathbf{MS})} (\mathbf{MS})^T}{\mathbf{1}_{n \times m} (\mathbf{MS})^T + \gamma' \mathbf{N}[\mathbf{NA}]^{\circ 3}}, \quad \mathbf{S} \leftarrow \mathbf{S} \circ \frac{(\mathbf{AM})^T \frac{\mathbf{X}}{(\mathbf{AM}) \mathbf{S}}}{(\mathbf{AM})^T \mathbf{1}_{n \times m}} \quad (34)$$

where  $\mathbf{1} \in \mathbb{R}^{n \times m}$  is a matrix whose all elements are one and the other notations are same as defined previously.

## 5. Algorithm Implementation

In this section, we will discuss several points related to the implementation of the proposed algorithm.

### 5.1. Initialization

Many algorithms had been designed in the past to enhance the initialization of the classical NMF problem. In this work, we utilize the Nonnegative Double Singular Value Decomposition (NNDSVD) algorithm [59] in order to initialize the matrices  $\mathbf{A}$  and  $\mathbf{S}$ . NNDSVD takes the HSI  $\mathbf{X}$  and the no. of endmembers  $r$  as the input and generates a pair of  $\mathbf{A}$  and  $\mathbf{S}$  matrices which could be utilized to initialize the proposed KbSNMF algorithm. The basic NNDSVD algorithm is based on two singular value decomposition (SVD) processes, first, approximating the data matrix and the second, approximating positive sections of the resulting partial SVD factors incorporating the properties of unit rank matrices. Extensive evidence can be found to suggest that NNDSVD promotes rapid convergence of the NMF algorithm.

### 5.2. Normalization

To avoid the complexity of computing  $\nabla_{\mathbf{A}} \overline{\mathbf{K}}$ , the endmember spectra are considered as signals of unit variance (See Section 3.3), which is not always true in HU setting. In order to rectify this premise, at the beginning of each iteration of the proposed algorithm, we normalize the endmember spectra by their individual variances (See Algorithm 1). Thus, the resulting algorithm follows the essence of projected multiplicative update methods which are often utilized in signal processing applications [24].

### 5.3. Convergence

Fig. 2 demonstrates the convergence of KbsNMF over iterations. Here, we have fixed the parameters  $\gamma$  and  $\theta$  at 3 and 0.4 respectively for KbsNMF-fnorm, and at 8 and 0.4 respectively for KbsNMF-div. Selection of suitable  $\gamma$  and  $\theta$  and their effects on the unmixing performance are extensively discussed in Section 6.3.1. Observing Fig. 2(a) and 2(b), it is evident that KbsNMF converges to a local minimum w.r.t.  $\mathbf{A}$  and  $\mathbf{S}$ . Also our primary objective of maximizing  $\overline{\mathbf{K}}$  has been achieved, and can be clearly seen in the Fig. 2(c) and 2(d). In the meantime, as seen in Fig. 2(e) and 2(f), frobenius norm and divergence respectively converges to local minima w.r.t.  $\mathbf{A}$  and  $\mathbf{S}$  which ensures the quality of approximation between  $\mathbf{X}$  and  $\mathbf{AMS}$ .

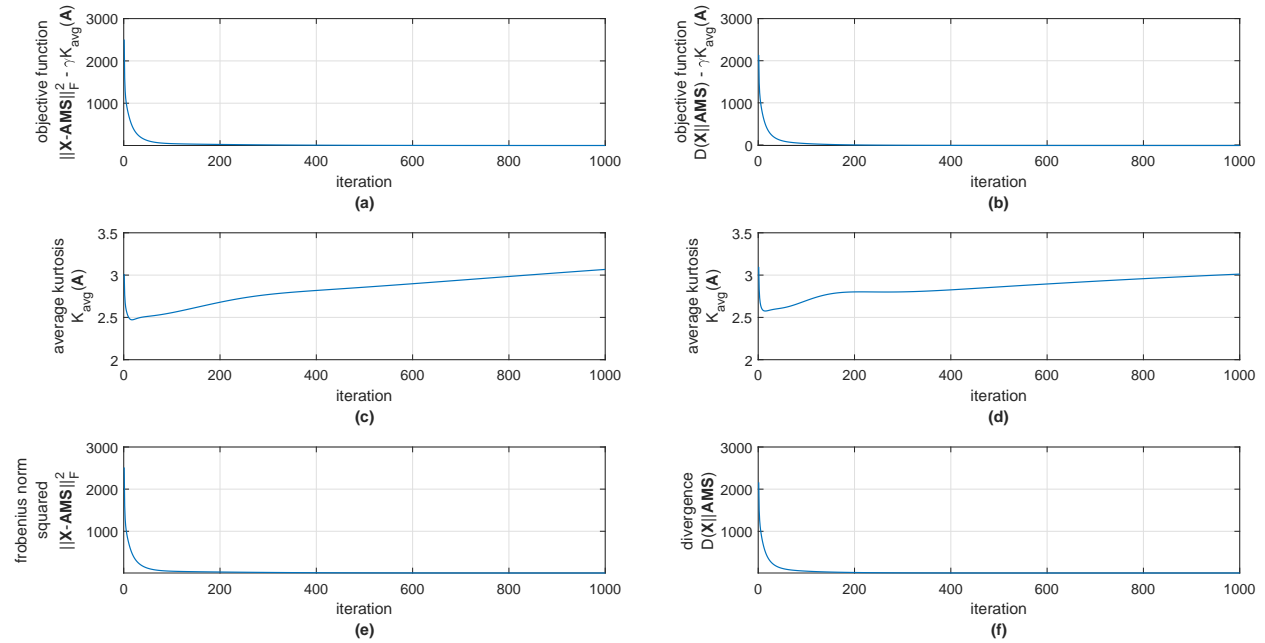


Figure 2: Convergence of the KbsNMF algorithm: Variation of (a) objective function, (c) average kurtosis of the extracted endmembers, and (e) square of frobenius norm between  $\mathbf{X}$  and  $\mathbf{AMS}$ , over iteration utilizing KbsNMF-fnorm algorithm. Variation of (b) objective function, (d) average kurtosis of the extracted endmembers, and (f) divergence of  $\mathbf{X}$  from  $\mathbf{AMS}$ , over iteration utilizing KbsNMF-div algorithm.

#### 5.4. Termination

In this work, we utilize two stopping criteria, one based on the maximum no. of iterations and the other based on the rate of change in the objective function. We choose a maximum no. of iterations,  $t_{max}$  and a minimum rate of change in the objective function  $C_{min}$ . The algorithm is terminated either if the present iteration  $t$  reaches  $t_{max}$  or if the present rate of change in the objective function  $C(t)$  falls below  $C_{min}$ . Here  $C(t) = \frac{|L(t-1)-L(t)|}{|L(t-1)|}$ , where  $L(t)$  is the value of the objective function at the  $t^{\text{th}}$  iteration. The selection of suitable  $t_{max}$  and  $C_{min}$  is discussed in Section 5.5.

#### 5.5. Parameter Selection

Observing Fig. 2(a) and 2(b), it is evident that both variations of KbsNMF algorithm have converged to local minima by the 1000<sup>th</sup> iteration. Thus, we fix  $t_{max}$  at 1000 preserving a reasonable allowance. Also it is seen that the percentage change in the objective function around the 1000<sup>th</sup> iteration is in the order of  $10^{-4}$ . Thus we fix  $C_{min}$  at  $10^{-5}$  to ensure convergence. Determining optimum control parameters  $\gamma$  and  $\theta$  is discussed in Section 6.3.1 via experiment. Adhering to all the implementing issues discussed above, the proposed KbsNMF algorithm can be summarized as in Algorithm 1.

## 6. Experiments and Discussions

### 6.1. Experimental Setting

The proposed algorithm is tested on simulated as well as real hyperspectral remote sensing data (See Sections 6.3 and 6.4). Also, we compare the performance of our proposed algorithm with five other popular state of the art NMF-based HU algorithms:  $l_{1/2}$ -NMF, SGSNMF, Min-vol NMF, R-CoNMF, and GNMF. To ensure that the evaluations are done on common grounds, we utilize the same initializing procedure and stopping criteria as mentioned in Sections 5.1 and 5.4 respectively, for all the competing algorithms.

### 6.2. Performance Criteria

In order to evaluate the performance of the proposed KbsNMF algorithm and assess its competitiveness with the other competing algorithms, we utilize two performance criteria, which are commonly adopted in HU performance evaluation, Spectral Angle Distance (SAD) and Root Mean Square Error (RMSE). In most of the previous literature on HU, SAD had been utilized to compare the extracted endmembers with the ground truth endmembers while RMSE had been utilized to compare the extracted abundance maps with the ground truth abundance maps. In our work  $SAD_i$ , as in (35) measures the spectral angle between the  $i^{\text{th}}$  ground truth endmember spectrum  $\mathbf{a}_i$  and the corresponding extracted endmember spectrum  $\hat{\mathbf{a}}_i$ , in radians;  $RMSE_i$ , as in (36) measures the difference between the  $i^{\text{th}}$  ground truth abundance matrix  $\mathbf{S}_i$  and the corresponding extracted abundance matrix  $\hat{\mathbf{S}}_i$ .

---

**Algorithm 1: KbSNMF Algorithm for HU**

---

**Input:**  $\mathbf{X}$ ,  $r$ ,  $\gamma$ ,  $\theta$ ,  $t_{max}$ , and  $C_{min}$ , *Algorithm*,

1 Initialize  $\mathbf{A}$  and  $\mathbf{S}$  utilizing NNDSVD algorithm [59];

2 Compute  $\mathbf{M}$  utilizing (25);

3 Compute  $\mathbf{N}$  as in (21);

4 Normalize each column of  $\mathbf{A}$  w.r.t its variance;

5 **while**  $t \leq t_{max} \wedge C \geq C_{min}$  **do**

6     Update  $\mathbf{A}$ :

7     **switch** *Algorithm* **do**

8         **case** *KbSNMF-fnorm* **do**

9              $\mathbf{A} \leftarrow \mathbf{A} \circ \frac{\mathbf{X}(\mathbf{MS})^T}{\mathbf{A}(\mathbf{MS})(\mathbf{MS})^T + \gamma' \mathbf{N}[\mathbf{NA}]^{\circ 3}};$

10         **end**

11         **case** *KbSNMF-div* **do**

12              $\mathbf{A} \leftarrow \mathbf{A} \circ \frac{\frac{\mathbf{X}}{\mathbf{A}(\mathbf{MS})}(\mathbf{MS})^T}{\mathbf{1}_{n \times m}(\mathbf{MS})^T + \gamma' \mathbf{N}[\mathbf{NA}]^{\circ 3}};$

13         **end**

14     **end**

15     Normalize each column of  $\mathbf{A}$  w.r.t its variance;

16     Update  $\mathbf{S}$ :

17     **switch** *Algorithm* **do**

18         **case** *KbSNMF-fnorm* **do**

19              $\mathbf{S} \leftarrow \mathbf{S} \circ \frac{(\mathbf{AM})^T \mathbf{X}}{(\mathbf{AM})^T (\mathbf{AM}) \mathbf{S}}$

20         **end**

21         **case** *KbSNMF-div* **do**

22              $\mathbf{S} \leftarrow \mathbf{S} \circ \frac{(\mathbf{AM})^T \frac{\mathbf{X}}{(\mathbf{AM}) \mathbf{S}}}{(\mathbf{AM})^T \mathbf{1}_{n \times m}}$

23         **end**

24     **end**

25 **end**

**Output:** Extracted  $\mathbf{A}$  and  $\mathbf{S}$

---

$$SAD_i = \cos^{-1} \left( \frac{\hat{\mathbf{a}}_i^T \mathbf{a}_i}{\|\hat{\mathbf{a}}_i\|_2 \|\mathbf{a}_i\|_2} \right) \quad (35)$$

$$RMSE_i = \sqrt{\frac{1}{m} \sum_{j=1}^m (\mathbf{s}_{ij} - \hat{\mathbf{s}}_{ij})^2} \quad (36)$$

### 6.3. Experiments on Simulated Data

An HSI dataset was simulated utilizing hyperspectral imagery synthesis toolbox (HSIST)<sup>5</sup> in MATLAB. HSIST consists of the full USGS spectral library<sup>6</sup> which contains hundreds of endmember spectra including minerals, organic and volatile compounds, vegetation, and man-made materials. Out of them, three endmember spectra consisting 480 spectral bands each were chosen and their corresponding abundance maps of size  $64 \times 64$  each were generated incorporating a spherical Gaussian field [60]. Fig. 3 illustrates the spectra of the selected endmembers: “seawater”, “clintonite”, “sodiumbicarbonate” and their corresponding abundance maps. The experiments discussed in this section

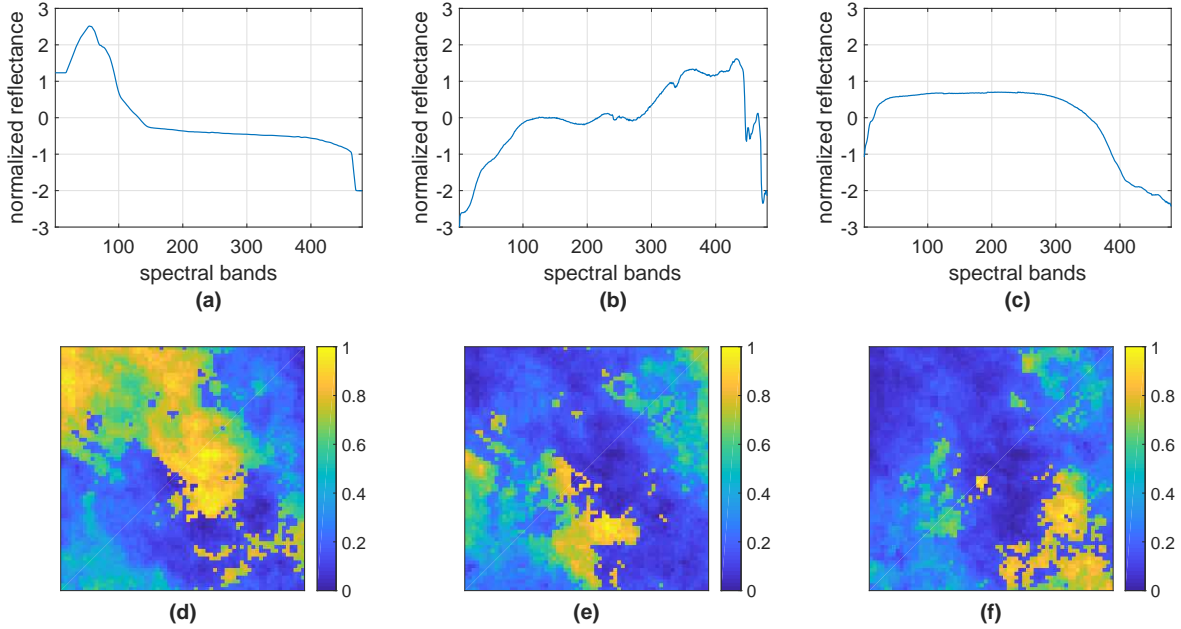


Figure 3: Endmember spectra from the USGS library, which are utilized to create the simulated HSI dataset along with their corresponding abundance maps: (a) endmember spectrum and (d) abundance map of “seawater”, (b) endmember spectrum and (e) abundance map of “clintonite”, and (c) endmember spectrum and (f) abundance map of “sodiumbicarbonate”.

<sup>5</sup>[http://www.ehu.es/ccwintco/index.php/Hyperspectral\\_Imagery\\_Synthesis\\_tools\\_for\\_MATLAB](http://www.ehu.es/ccwintco/index.php/Hyperspectral_Imagery_Synthesis_tools_for_MATLAB)

<sup>6</sup><http://speclab.cr.usgs.gov/spectral-lib.html>



### 6.3.1. Sensitivity to control parameters

We conduct experiments to find optimum values for  $\gamma$  and  $\theta$  for KbSNMF-fnorm and KbSNMF-div. We increase  $\gamma$  from 0 to 25 in steps of 1, increase  $\theta$  from 0 to 1 in steps of 0.1, and evaluate the unmixing performance at each step. Note that the SAD values in Fig. 4 are average values over all extracted endmembers. It is seen that SAD reaches minimum around  $\gamma = 3$  and  $\theta = 0.4$  in Fig. 4(a) and around  $\gamma = 8$  and  $\theta = 0.4$  in Fig. 4(b). Thus we fix  $\gamma$  and  $\theta$  at 3 and 0.4 respectively for KbSNMF-fnorm and at 8 and 0.4 respectively for KbSNMF-div.

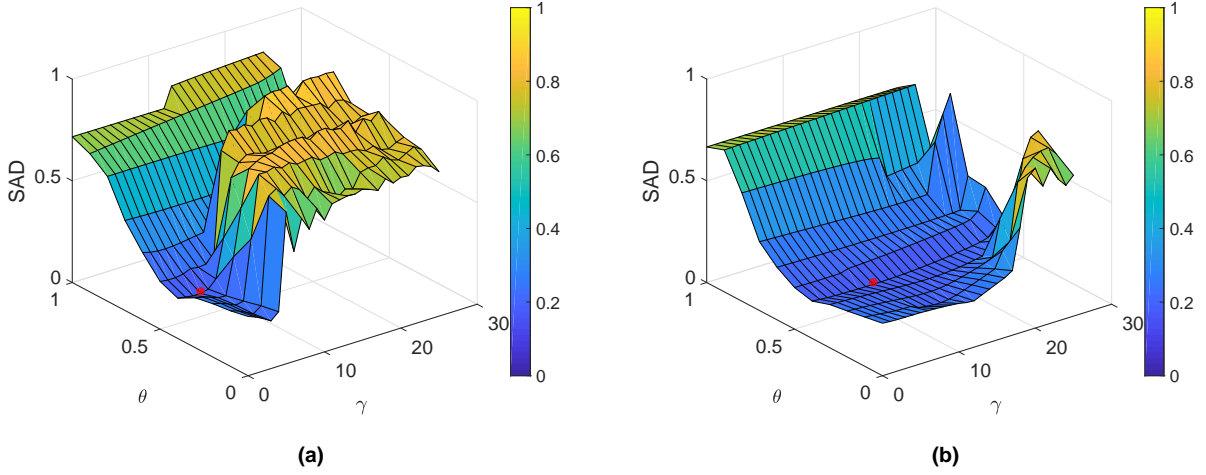


Figure 4: Variation of unmixing performance w.r.t. SAD with  $\gamma$  and  $\theta$  for (a) KbSNMF-fnorm and (b) KbSNMF-div. The minimum SAD value in each 3-D surface is marked in red.

### 6.3.2. Unmixing performance

Under this experiment, we compare the unmixing performance of KbSNMF with the other HU algorithms mentioned in Section 6.1 in terms of SAD and RMSE. Table 1 shows SAD values for each extracted endmember and Table 2 shows RMSE values for each extracted abundance map, under the different methods. It is clearly seen that the KbSNMF under its both variations dominates the other competing algorithms w.r.t SAD while signifying competitive performance w.r.t RMSE. Fig. 5 and 6 respectively illustrates the endmember spectra and abundance maps extracted via KbSNMF along with their ground truths.

### 6.3.3. Robustness to noise

In this experiment, we aim to analyze how the proposed algorithm performs under noisy environments. We add zero-mean white Gaussian noise to the original noise-free simulated dataset with a predetermined signal to noise ratio (SNR) given by (37).

$$\text{SNR} = 10 \log_{10} \frac{\mathbb{E}(\mathbf{x}^T \mathbf{x})}{\mathbb{E}(\mathbf{n}^T \mathbf{n})} \quad (37)$$

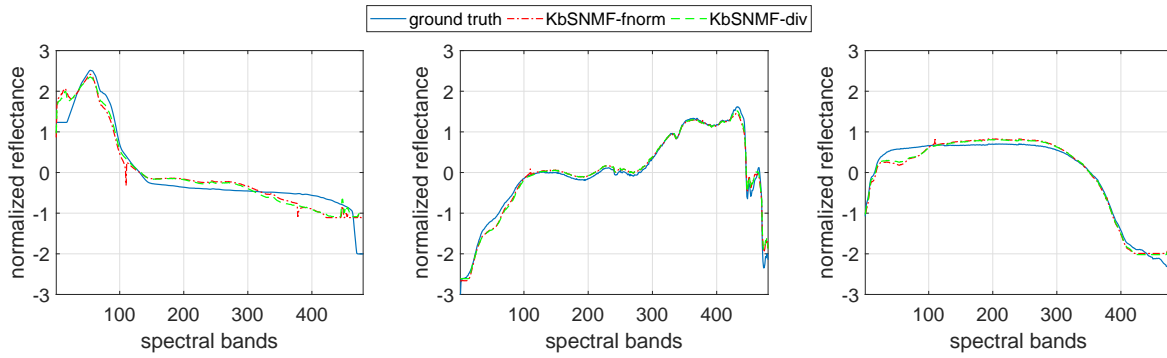


Figure 5: Endmembers extracted by KbSNMF from simulated dataset: “seawater”, “clintonite” and “sodiumbicarbonate” respectively.

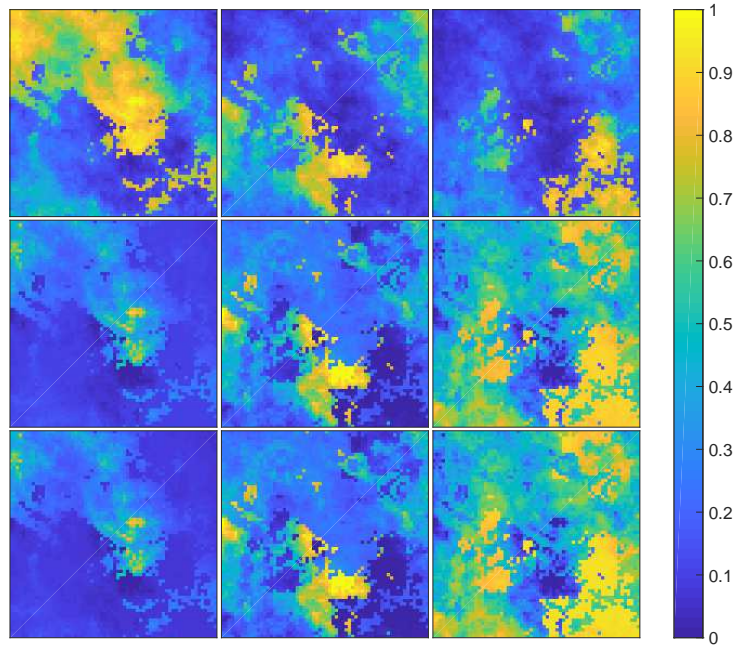


Figure 6: Abundance maps extracted by KbSNMF from simulated dataset: *Top row*- ground truth abundance maps, *Middle row*- extracted abundance maps by KbSNMF-fnorm, *Bottom row*- extracted abundance maps by KbSNMF-div.

Here  $\mathbf{x}$  is the pixel spectrum vector,  $\mathbf{n}$  is the noise signal vector, and  $\mathbb{E}$  is the expectation operator. We conduct the experiment under 11 SNR levels: 0dB, 5dB, 10dB, 15dB, 20dB, 25dB, 30dB, 35dB, 40dB, 45dB, 50dB and the results are illustrated in Fig. 7 w.r.t. SAD and RMSE. Clearly KbSNMF-fnorm and KbSNMF-div report the best performance w.r.t SAD showing superior performance over competing algorithms at almost all the considered noise levels. They also show some robustness to noise up until 30dB. In terms of RMSE, both KbSNMF-fnorm and KbSNMF-div show some robustness to noise up until 20dB and gradually deteriorate performance with noise thereafter. However, both KbSNMF-fnorm and KbSNMF-div outperform GNMf at all noise levels w.r.t. RMSE. The superior performance of KbSNMF-fnorm and KbSNMF-div w.r.t to SAD is due to the novel auxiliary constraint on the endmember matrix and thereby attempting to extract most realistic constituent spectra

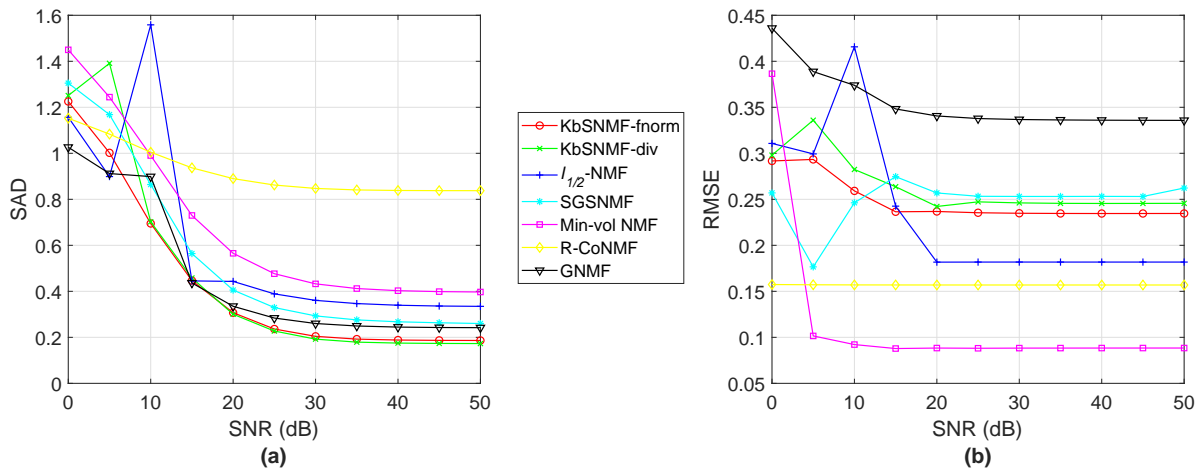


Figure 7: Variation of (a) SAD and (b) RMSE with the noise level of the simulated datasets

#### 6.3.4. Sensitivity to number of pixels

Within this experiment, we illustrate how the proposed algorithm performs under simulated HSI datasets of different nos. of pixels. The no. of pixels in a HSI is a major concern since it denotes the amount of statistical information in the input to the algorithm. The amount of statistical information presented to a numerical algorithm determines the tendency of an algorithm to be trapped in a local minima [61]. Utilizing the HSIST, with the same endmembers in Fig. 3, we generate 5 simulated datasets of size  $8 \times 8$ ,  $16 \times 16$ ,  $32 \times 32$ ,  $64 \times 64$ ,  $128 \times 128$  pixels. Fig. 8 illustrate the results w.r.t. SAD and RMSE. The unmixing performance of KbSNMF-fnorm and KbSNMF-div improves w.r.t. SAD with no. of pixels and even outperforms all competing algorithms when the no. of pixels are very high, *i.e.*  $64 \times 64$  and  $128 \times 128$  pixels. In terms of RMSE, KbSNMF-fnorm and KbSNMF-div outperform SGSNMF and GNMf when the no. of pixels are very high, *i.e.*  $64 \times 64$  and  $128 \times 128$  pixels.

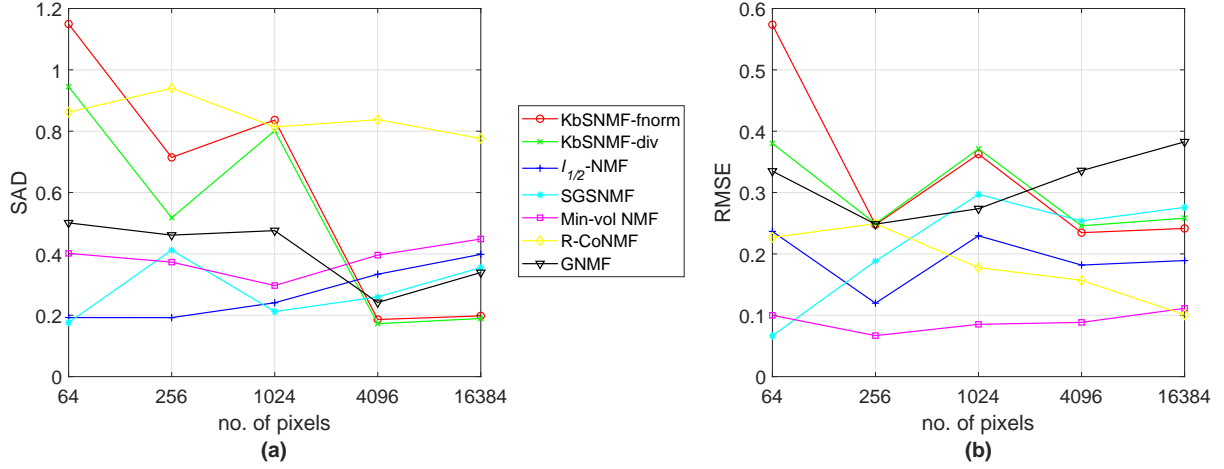


Figure 8: Variation of (a) SAD and (b) RMSE with the no. of pixels of the simulated datasets

### 6.3.5. Sensitivity to number of spectral bands

Here we vary the no. of spectral bands of the endmembers and observe the unmixing performance of the algorithms. We utilize the HSIST to generate 15 datasets constituting the same set of endmembers as in Fig. 3, but with different spectral resolutions, *i.e.* by increasing  $n$  from 120 to 960 in steps of 60. We also incorporate the same set of abundance maps in order to preserve impartiality. The results are shown in Fig. 9. KbSNMF-fnorm and KbSNMF-div outperform all the other algorithms w.r.t. SAD for almost all levels of no. of spectral bands. However, the performance of KbSNMF-fnorm and KbSNMF-div deteriorate drastically w.r.t SAD for very low no. of spectral bands, *i.e.* around 200 spectral bands. In terms of RMSE, KbSNMF-fnorm and KbSNMF-div outperforms GNMF at all levels of no. of spectral bands and outperform SGSNMF at low levels of no. of spectral bands, *i.e.* below 480 spectral bands.

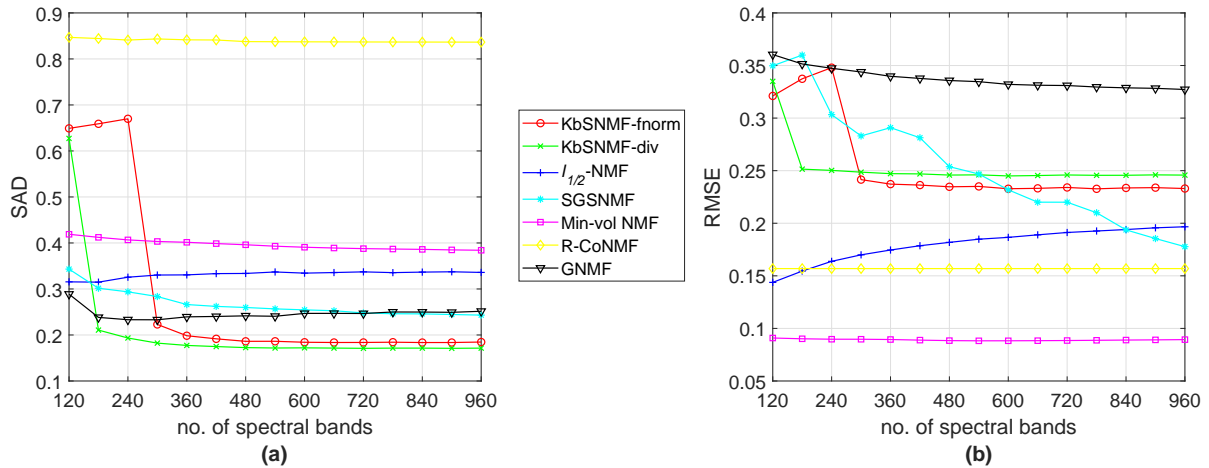


Figure 9: Variation of (a) SAD and (b) RMSE with the no. of spectral bands of the simulated datasets

### 6.3.6. Sensitivity to number of endmembers

In this experiment, we vary the no. of endmembers and investigate the performance of the algorithms. 9 dataset are simulated by picking different spectra from the USGS spectral library, but with the same no. of spectral bands (480 spectral bands), *i.e.* we increase  $r$  from 2 to 9 in steps of 1. The results are illustrated in Fig. 10. All the algorithms have the tendency to deteriorate performance w.r.t. SAD with the no. of endmembers. KbsNMF-fnorm and KbsNMF-div outperform R-CoNMF when the no. of endmembers are low, *i.e.* below 7 endmembers, outperform SGSNMF when the no. of endmembers are high, *i.e.* above 5 endmembers. In terms of RMSE, KbsNMF-fnorm and KbsNMF-div outperform SGSNMF and GNMF when the no. of endmembers are low, *i.e.* below 4 endmembers.

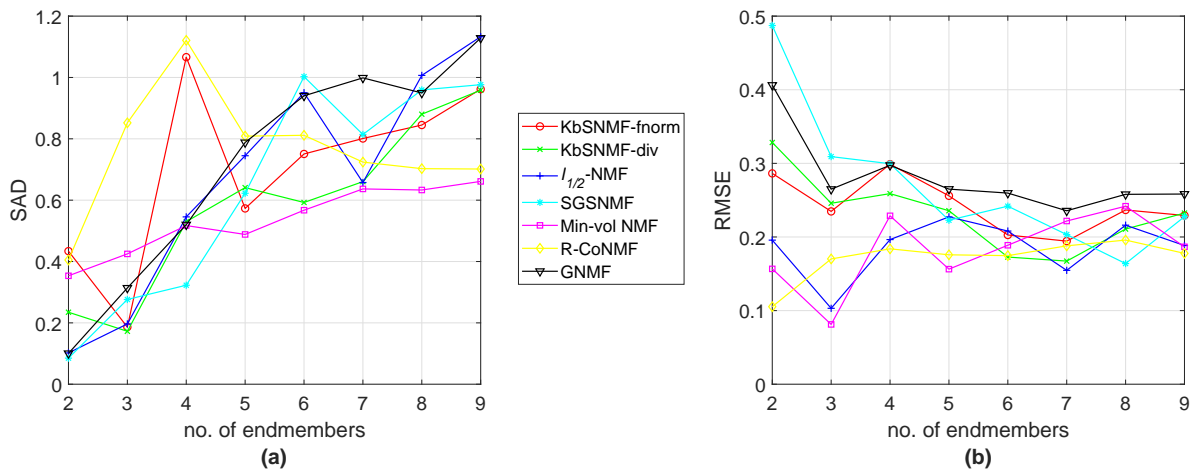


Figure 10: Variation of (a) SAD and (b) RMSE with the no. of endmembers of the simulated datasets

### 6.4. Experiments on Real Data

To assess the performance of the proposed algorithm on real environments, we conduct experiments on real hyperspectral remote sensing datasets. We chose the Samson dataset which is a widely utilized landmark HSI for performance evaluation and comparison in HU studies. Since Samson scene is a very large HSI and difficult to process, we choose a  $95 \times 95$  pixels region for our analysis. Each pixel is recorded at 156 spectral channels covering wavelengths from 401 nm to 889 nm. The spectral resolution of the HSI is up to 3.13 nm. Unlike other landmark real HSI datasets, Samson dataset is not degraded by any blank or noisy channels.

The Samson dataset consists of three constituent spectra, *i.e.* “Soil”, “Tree” and “Water”. Fig. 11 illustrates the spectra of the constituent endmembers and the top row of Fig. 12 illustrates their corresponding abundance maps. The ground truths for real HSI data are worked out utilizing a procedure similar to that of [62] and [63]. First, the Virtual Dimensionality (VD) algorithm [64] is utilized to determine the no. of constituent endmembers of the HSI. Second, the pixels that contain pure constituent endmembers are chosen manually in accordance with the USGS mineral spectral library. Finally, the corresponding abundances are computed utilizing the CVX optimization Toolbox

in MATLAB. Accordingly-generated ground truths are often utilized in HU algorithm evaluation and comparison, and are readily-available<sup>7</sup>.

We compare the unmixing performance of KbSNMF with the other competing algorithms w.r.t SAD and RMSE for the Samson dataset. Table 3 shows SAD values for each extracted endmember and Table 4 shows RMSE values for each extracted abundance map, under the different methods. In terms of average SAD, R-CoNMF outperforms all algorithms. However, KbSNMF-fnorm and KbSNMF-div outperform rest of the other algorithms. Also KbSNMF-div reports the best performance w.r.t. SAD in extracting the endmember “water”. In terms of RMSE, Min-vol NMF and SGSNMF outperform all algorithms. KbSNMF-div reports the third best average performance w.r.t. RMSE. The endmember spectra extracted by KbSNMF-fnorm and KbSNMF-div are shown in Fig. 11, and it can be observed that they closely follow their ground truth spectra. Also, the abundance maps extracted by KbSNMF-fnorm and KbSNMF-div are shown in Fig. 12, and it is evident that KbSNMF-div has managed to accurately extract the abundance maps.

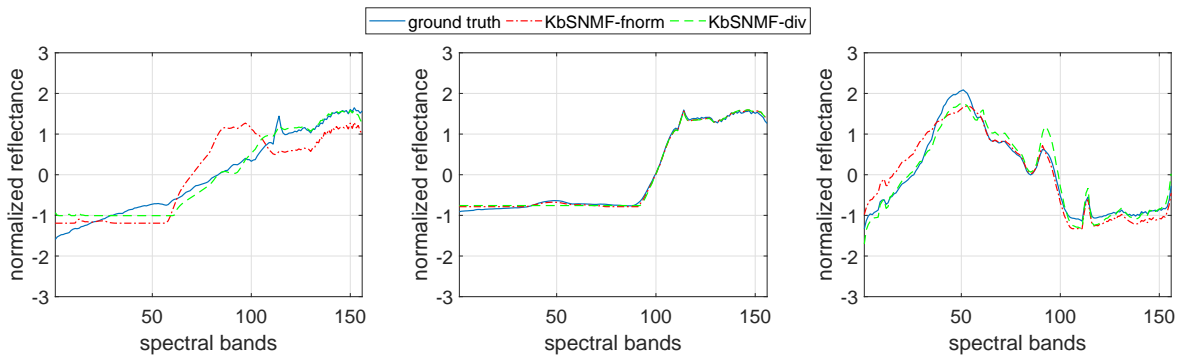


Figure 11: Endmember spectra extracted by KbSNMF of Samson dataset: “Soil”, “Tree” and “Water” respectively.

## 7. Conclusion

In this paper, a novel blind HU algorithm called KbSNMF is proposed. The algorithm is based on incorporating the independence of endmembers to the conventional NMF framework. Based on this consideration, a novel constraint called the kurtosis constraint is introduced. This constraint is based on the fourth central moment of a signal which signifies the statistical independence of the underlying signal. In this paper, a comprehensive derivation of the proposed algorithm is included along with its performance evaluation in simulated as well as real environments. This paper also provides a performance comparison of the proposed algorithm with the other state of the art blind NMF-based HU algorithms. Moreover, experimental results verify that dominant performance in endmember extraction can be obtained through the introduction of the kurtosis constraint. Hence the proposed algorithm can be effectively utilized to extract accurate endmembers which can then be passed through as supervisory input data to modern DL methods.

<sup>7</sup>[http://www.escience.cn/people/feiyunZHU/Dataset\\_GT.html](http://www.escience.cn/people/feiyunZHU/Dataset_GT.html)

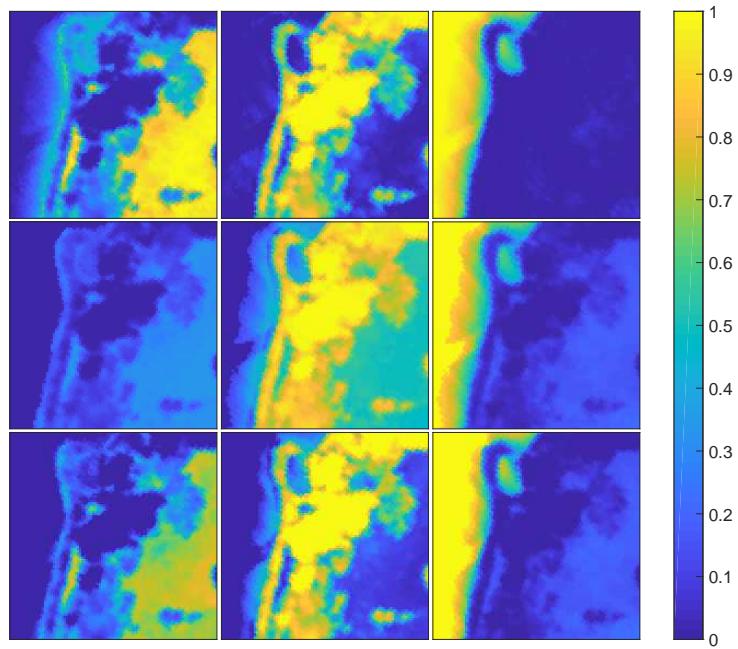


Figure 12: Results of Samson dataset: *Top row*- ground truth abundance maps, *Middle row*- extracted abundance maps by KbSNMF-fnorm. *Bottom row*- extracted abundance maps by KbSNMF-div.

Methods	KbSNMF-fnorm	KbSNMF-div	$l_{1/2}$ -NMF	SGSNMF	Min-vol NMF	R-CoNMF	GNMF
Seawater	<i>0.3000</i>	<b>0.2746</b>	0.6855	0.5416	0.8891	1.7408	<u>0.3179</u>
Clintonite	<b>0.1078</b>	<i>0.1119</i>	0.2990	<u>0.2288</u>	0.2803	0.7109	0.3523
Sodiumbicarbonate	0.1508	0.1311	<u>0.0168</u>	<b>0.0090</b>	<i>0.0188</i>	0.0614	0.0547
Average	<i>0.1862</i>	<b>0.1725</b>	0.3337	0.2598	0.3961	0.8377	<u>0.2416</u>

Table 1: Unmixing performance comparison w.r.t. SAD for simulated dataset. The best performances are in bold typeface, the second best performances are italicized, and the third best performances are underlined.

Methods	KbSNMF-fnorm	KbSNMF-div	$l_{1/2}$ -NMF	SGSNMF	Min-vol NMF	R-CoNMF	GNMF
Seawater	0.3049	0.3190	<u>0.2488</u>	0.3579	<b>0.1052</b>	<i>0.1753</i>	0.4001
Clintonite	<u>0.1195</u>	0.1200	<b>0.0573</b>	0.2906	<i>0.0854</i>	0.1473	0.1668
Sodiumbicarbonate	0.2797	0.2985	0.2394	<i>0.1123</i>	<b>0.0745</b>	<u>0.1475</u>	0.4403
Average	0.2347	0.2458	<u>0.1818</u>	0.2538	<b>0.0884</b>	<i>0.1569</i>	0.3357

Table 2: Unmixing performance comparison w.r.t. RMSE for simulated dataset. The best performances are in bold typeface, the second best performances are italicized, and the third best performances are underlined.

Methods	KbSNMF-fnorm	KbSNMF-div	$l_{1/2}$ -NMF	SGSNMF	Min-vol NMF	R-CoNMF	GNMF
Soil	0.4975	<i>0.2078</i>	<u>0.3455</u>	0.3743	0.3463	<b>0.1253</b>	0.3497
Tree	<i>0.0456</i>	<u>0.0647</u>	0.1433	0.1721	0.2315	<b>0.0105</b>	0.0984
Water	<u>0.2771</u>	<b>0.2014</b>	0.3513	0.2941	<i>0.2429</i>	0.3219	0.4298
Average	<u>0.2734</u>	<i>0.1580</i>	0.2800	0.2802	0.2736	<b>0.1526</b>	0.2926

Table 3: Unmixing performance comparison w.r.t. SAD for Samson dataset. The best performances are in bold typeface, the second best performances are italicized, and the third best performances are underlined.

Methods	KbSNMF-fnorm	KbSNMF-div	$l_{1/2}$ -NMF	SGSNMF	Min-vol NMF	R-CoNMF	GNMF
Soil	0.3429	0.1574	0.4217	<i>0.0532</i>	<u>0.0967</u>	<b>0.0431</b>	0.3832
Tree	0.2673	0.0911	<i>0.0432</i>	<u>0.0882</u>	0.1245	<b>0.0118</b>	0.0325
Water	<i>0.0910</i>	<u>0.0927</u>	0.2359	0.1432	<b>0.0432</b>	0.5321	0.1654
Average	0.2337	<u>0.1137</u>	0.2336	<i>0.0949</i>	<b>0.0881</b>	0.1957	0.1937

Table 4: Unmixing performance comparison w.r.t. RMSE for Samson dataset. The best performances are in bold typeface, the second best performances are italicized, and the third best performances are underlined.



## References

- [1] H. Huang, Y. Duan, H. He, G. Shi, F. Luo, Spatial-spectral local discriminant projection for dimensionality reduction of hyperspectral data, *ISPRS Journal of Photogrammetry and Remote Sensing* 156 (2019) 77 – 93.  
doi:<https://doi.org/10.1016/j.isprsjprs.2019.06.018>.  
URL <http://www.sciencedirect.com/science/article/pii/S0924271619301595>
- [2] M. Paoletti, J. Haut, J. Plaza, A. Plaza, Deep learning classifiers for hyperspectral imaging: A review, *ISPRS Journal of Photogrammetry and Remote Sensing* 158 (2019) 279 – 317.  
doi:<https://doi.org/10.1016/j.isprsjprs.2019.09.006>.  
URL <http://www.sciencedirect.com/science/article/pii/S0924271619302187>
- [3] A. Appice, D. Malerba, Segmentation-aided classification of hyperspectral data using spatial dependency of spectral bands, *ISPRS Journal of Photogrammetry and Remote Sensing* 147 (2019) 215 – 231.  
doi:<https://doi.org/10.1016/j.isprsjprs.2018.11.023>.  
URL <http://www.sciencedirect.com/science/article/pii/S0924271618303253>
- [4] J. P. Rivera-Caicedo, J. Verrelst, J. Muñoz-Mar, G. Camps-Valls, J. Moreno, Hyperspectral dimensionality reduction for biophysical variable statistical retrieval, *ISPRS Journal of Photogrammetry and Remote Sensing* 132 (2017) 88 – 101.  
doi:<https://doi.org/10.1016/j.isprsjprs.2017.08.012>.  
URL <http://www.sciencedirect.com/science/article/pii/S092427161730179X>
- [5] R. D. M. Scafutto, C. R. de Souza Filho, W. J. de Oliveira, Hyperspectral remote sensing detection of petroleum hydrocarbons in marine environments, *ISPRS Journal of Photogrammetry and Remote Sensing* 128 (2017) 146 – 157.  
doi:<https://doi.org/10.1016/j.isprsjprs.2017.03.009>.  
URL <http://www.sciencedirect.com/science/article/pii/S0924271616301319>
- [6] I. Makki, R. Younes, C. Francis, T. Bianchi, M. Zucchetti, A survey of landmine detection using hyperspectral imaging, *ISPRS Journal of Photogrammetry and Remote Sensing* 124 (2017) 40 – 53.  
doi:<https://doi.org/10.1016/j.isprsjprs.2016.12.009>.  
URL <http://www.sciencedirect.com/science/article/pii/S0924271616306451>
- [7] S. Song, W. Gong, B. Zhu, X. Huang, Wavelength selection and spectral discrimination for paddy rice, with laboratory measurements, *ISPRS Journal of Photogrammetry and Remote Sensing* 66 (5) (2011) 672 – 682.  
doi:<https://doi.org/10.1016/j.isprsjprs.2011.05.002>.  
URL <http://www.sciencedirect.com/science/article/pii/S0924271611000682>

- [8] B. Fei, Chapter 3.6 - hyperspectral imaging in medical applications, in: J. M. Amigo (Ed.), *Hyperspectral Imaging*, Vol. 32 of *Data Handling in Science and Technology*, Elsevier, 2020, pp. 523 – 565. doi:<https://doi.org/10.1016/B978-0-444-63977-6.00021-3>. URL <http://www.sciencedirect.com/science/article/pii/B9780444639776000213>
- [9] S. Vithana, E. Ekanayake, E. Ekanayake, A. Rathnayake, G. Jayatilaka, H. Herath, G. Godaliyadda, M. Ekanayake, Adaptive hierarchical clustering for hyperspectral image classification: Umbrella clustering, *Journal of Spectral Imaging* 8 (1) (2019) a1. doi:[10.1255/jsi.2019.a11](https://doi.org/10.1255/jsi.2019.a11). URL <https://doi.org/10.1255/jsi.2019.a11>
- [10] B. Rathnayake, E. Ekanayake, K. Weerakoon, G. Godaliyadda, M. Ekanayake, H. Herath, Graph-based blind hyperspectral unmixing via nonnegative matrix factorization.
- [11] J. Gao, B. Meng, T. Liang, Q. Feng, J. Ge, J. Yin, C. Wu, X. Cui, M. Hou, J. Liu, H. Xie, Modeling alpine grassland forage phosphorus based on hyperspectral remote sensing and a multi-factor machine learning algorithm, *ISPRS Journal of Photogrammetry and Remote Sensing* 147 (2019) 104 – 117. doi:<https://doi.org/10.1016/j.isprsjprs.2018.11.015>. URL <http://www.sciencedirect.com/science/article/pii/S0924271618303113>
- [12] E. M. M. B. Ekanayake, E. M. H. E. B. Ekanayake, A. R. M. A. N. Rathnayake, S. S. P. Vithana, H. M. V. R. Herath, G. M. R. I. Godaliyadda, M. P. B. Ekanayake, A semi-supervised algorithm to map major vegetation zones using satellite hyperspectral data, in: *2018 9th Workshop on Hyperspectral Image and Signal Processing: Evolution in Remote Sensing (WHISPERS)*, 2018, pp. 1–5. doi:[10.1109/WHISPERS.2018.8747025](https://doi.org/10.1109/WHISPERS.2018.8747025).
- [13] E. Ekanayake, S. Vithana, E. Ekanayake, A. Rathnayake, A. Abeysekara, T. Oorloff, H. Herath, G. Godaliyadda, M. Ekanayake, A. Senaratne, Mapping ilmenite deposit in pulmudai, sri lanka using a hyperspectral imaging-based surface mineral mapping method, *Journal of the National Science Foundation of Sri Lanka* 47 (3) (2019) 271284. doi:<http://doi.org/10.4038/jnsfsl.v47i3.9276>. URL <https://jnsfsl.sljol.info/articles/abstract/10.4038/jnsfsl.v47i3.9276/#>
- [14] X. Xu, Z. Shi, Multi-objective based spectral unmixing for hyperspectral images, *ISPRS Journal of Photogrammetry and Remote Sensing* 124 (2017) 54 – 69. doi:<https://doi.org/10.1016/j.isprsjprs.2016.12.010>. URL <http://www.sciencedirect.com/science/article/pii/S0924271616306529>
- [15] N. Keshava, J. Mustard, Spectral unmixing, *IEEE Signal Processing Magazine* (2002). URL <https://academic.microsoft.com/paper/2295820431>

- [16] X. Xu, Z. Shi, B. Pan, l0-based sparse hyperspectral unmixing using spectral information and a multi-objectives formulation, *ISPRS Journal of Photogrammetry and Remote Sensing* 141 (2018) 46 – 58.  
doi:<https://doi.org/10.1016/j.isprsjprs.2018.04.008>.  
URL <http://www.sciencedirect.com/science/article/pii/S0924271618301163>
- [17] Y. Zhong, X. Wang, L. Zhao, R. Feng, L. Zhang, Y. Xu, Blind spectral unmixing based on sparse component analysis for hyperspectral, *ISPRS Journal of Photogrammetry and Remote Sensing* 119 (2016) 49 – 63.  
doi:<https://doi.org/10.1016/j.isprsjprs.2016.04.008>.  
URL <http://www.sciencedirect.com/science/article/pii/S092427161630048X>
- [18] R. Feng, Y. Zhong, L. Zhang, Adaptive non-local euclidean medians sparse unmixing for hyperspectral imagery, *ISPRS Journal of Photogrammetry and Remote Sensing* 97 (2014) 9 – 24.  
doi:<https://doi.org/10.1016/j.isprsjprs.2014.07.009>.  
URL <http://www.sciencedirect.com/science/article/pii/S0924271614001920>
- [19] F. Zhu, Y. Wang, S. Xiang, B. Fan, C. Pan, Structured sparse method for hyperspectral unmixing, *ISPRS Journal of Photogrammetry and Remote Sensing* 88 (2014) 101 – 118.  
doi:<https://doi.org/10.1016/j.isprsjprs.2013.11.014>.  
URL <http://www.sciencedirect.com/science/article/pii/S0924271613002761>
- [20] C. Zhang, Q. Qin, T. Zhang, Y. Sun, C. Chen, Endmember extraction from hyperspectral image based on discrete firefly algorithm, *ISPRS Journal of Photogrammetry and Remote Sensing* 126 (2017) 108 – 119.  
doi:<https://doi.org/10.1016/j.isprsjprs.2017.02.005>.  
URL <http://www.sciencedirect.com/science/article/pii/S0924271616301538>
- [21] W. Sun, J. Ma, G. Yang, B. Du, L. Zhang, A poisson nonnegative matrix factorization method with parameter subspace clustering, *ISPRS Journal of Photogrammetry and Remote Sensing* 128 (2017) 27 – 39.  
doi:<https://doi.org/10.1016/j.isprsjprs.2017.03.004>.  
URL <http://www.sciencedirect.com/science/article/pii/S0924271616303860>
- [22] M. Parente, A. Plaza, Survey of geometric and statistical unmixing algorithms for hyperspectral images, in: *2010 2nd Workshop on Hyperspectral Image and Signal Processing: Evolution in Remote Sensing, 2010*, pp. 1–4.  
doi:[10.1109/WHISPERS.2010.5594929](https://doi.org/10.1109/WHISPERS.2010.5594929).
- [23] Lifan Liu, Bin Wang, Liming Zhang, Jian Qiu Zhang, Decomposition of mixed pixels using bayesian self-organizing map (bsom) neural networks, in: *2007 IEEE International Geoscience and Remote Sensing Symposium, 2007*, pp. 2014–2017. doi:[10.1109/IGARSS.2007.4423225](https://doi.org/10.1109/IGARSS.2007.4423225).
- [24] J. V. Stone, *Independent Component Analysis: A Tutorial Introduction*, MIT Press, Cambridge, MA, USA, 2004.

- [25] J. Wang, C. . Chang, Applications of independent component analysis in endmember extraction and abundance quantification for hyperspectral imagery, *IEEE Transactions on Geoscience and Remote Sensing* 44 (9) (2006) 2601–2616. doi:10.1109/TGRS.2006.874135.
- [26] J. M. P. Nascimento, J. M. B. Dias, Does independent component analysis play a role in unmixing hyperspectral data?, *IEEE Transactions on Geoscience and Remote Sensing* 43 (1) (2005) 175–187. doi:10.1109/TGRS.2004.839806.
- [27] J. M. P. Nascimento, J. M. Bioucas-Dias, Hyperspectral unmixing algorithm via dependent component analysis, in: *2007 IEEE International Geoscience and Remote Sensing Symposium*, 2007, pp. 4033–4036. doi:10.1109/IGARSS.2007.4423734.
- [28] A. Plaza, P. Martinez, R. Perez, J. Plaza, Spatial/spectral endmember extraction by multidimensional morphological operations, *IEEE Transactions on Geoscience and Remote Sensing* 40 (9) (2002) 2025–2041. doi:10.1109/TGRS.2002.802494.
- [29] D. Rogge, B. Rivard, J. Zhang, A. Sanchez, J. Harris, J. Feng, Integration of spatialspectral information for the improved extraction of endmembers, *Remote Sensing of Environment* 110 (3) (2007) 287 – 303. doi:https://doi.org/10.1016/j.rse.2007.02.019. URL <http://www.sciencedirect.com/science/article/pii/S0034425707000934>
- [30] J. M. P. Nascimento, J. M. B. Dias, Vertex component analysis: a fast algorithm to unmix hyperspectral data, *IEEE Transactions on Geoscience and Remote Sensing* 43 (4) (2005) 898–910. doi:10.1109/TGRS.2005.844293.
- [31] M. D. Craig, Minimum-volume transforms for remotely sensed data, *IEEE Transactions on Geoscience and Remote Sensing* 32 (3) (1994) 542–552. doi:10.1109/36.297973.
- [32] J. M. Bioucas-Dias, A variable splitting augmented lagrangian approach to linear spectral unmixing, in: *2009 First Workshop on Hyperspectral Image and Signal Processing: Evolution in Remote Sensing*, 2009, pp. 1–4. doi:10.1109/WHISPERS.2009.5289072.
- [33] J. H. Bowles, P. J. Palmadesso, J. A. Antoniadis, M. M. Baumbach, L. J. Rickard, Use of filter vectors in hyperspectral data analysis, in: M. Strojnik, B. F. Andresen (Eds.), *Infrared Spaceborne Remote Sensing III*, Vol. 2553, International Society for Optics and Photonics, SPIE, 1995, pp. 148 – 157. doi:10.1117/12.221352. URL <https://doi.org/10.1117/12.221352>

- [34] N. R. A., S. K., S. T., L. J., H. P., Automatic endmember extraction from hyperspectral data for mineral exploration, in: Fourth International Airborne Remote Sensing Conference and Exhibition / 21st Canadian Symposium on Remote Sensing, Ottawa, Ontario, Canada, 1999, pp. 21–24.
- [35] D. Lee, H. Seung, Algorithms for non-negative matrix factorization, in: Advances in Neural Information Processing Systems 13 - Proceedings of the 2000 Conference, NIPS 2000, Advances in Neural Information Processing Systems, Neural information processing systems foundation, 2001.
- [36] X. Zhang, Y. Sun, J. Zhang, P. Wu, L. Jiao, Hyperspectral unmixing via deep convolutional neural networks, IEEE Geoscience and Remote Sensing Letters 15 (11) (2018) 1755–1759. doi:10.1109/LGRS.2018.2857804.
- [37] M. Wang, M. Zhao, J. Chen, S. Rahardja, Nonlinear unmixing of hyperspectral data via deep autoencoder networks, IEEE Geoscience and Remote Sensing Letters 16 (9) (2019) 1467–1471. doi:10.1109/LGRS.2019.2900733.
- [38] J. Li, X. Li, B. Huang, L. Zhao, Hopfield neural network approach for supervised nonlinear spectral unmixing, IEEE Geoscience and Remote Sensing Letters 13 (7) (2016) 1002–1006. doi:10.1109/LGRS.2016.2560222.
- [39] Z. Mitraka, F. Del Frate, F. Carbone, Spectral unmixing of urban landsat imagery by means of neural networks, in: 2015 Joint Urban Remote Sensing Event (JURSE), 2015, pp. 1–4. doi:10.1109/JURSE.2015.7120463.
- [40] G. A. Licciardi, F. Del Frate, Pixel unmixing in hyperspectral data by means of neural networks, IEEE Transactions on Geoscience and Remote Sensing 49 (11) (2011) 4163–4172. doi:10.1109/TGRS.2011.2160950.
- [41] D. D. Lee, H. S. Seung, Learning the parts of objects by non-negative matrix factorization, Nature 401 (6755) (1999) 788–791. doi:10.1038/44565.  
URL <https://doi.org/10.1038/44565>
- [42] Y. Qian, S. Jia, J. Zhou, A. Robles-Kelly, Hyperspectral unmixing via  $l_{1/2}$  sparsity-constrained nonnegative matrix factorization, IEEE Transactions on Geoscience and Remote Sensing 49 (11) (2011) 4282–4297. doi:10.1109/TGRS.2011.2144605.
- [43] A. Pascual-Montano, J. M. Carazo, K. Kochi, D. Lehmann, R. D. Pascual-Marqui, Nonsmooth nonnegative matrix factorization (nsnmf), IEEE Transactions on Pattern Analysis and Machine Intelligence 28 (3) (2006) 403–415. doi:10.1109/TPAMI.2006.60.
- [44] V. Leplat, A. M. S. Ang, N. Gillis, Minimum-volume rank-deficient nonnegative matrix factorizations, in: ICASSP 2019 - 2019 IEEE International Conference on Acoustics, Speech and Signal Processing (ICASSP), 2019, pp. 3402–3406. doi:10.1109/ICASSP.2019.8682280.

- [45] J. Li, J. M. Bioucas-Dias, A. Plaza, L. Liu, Robust collaborative nonnegative matrix factorization for hyperspectral unmixing, *IEEE Transactions on Geoscience and Remote Sensing* 54 (10) (2016) 6076–6090. doi:10.1109/TGRS.2016.2580702.
- [46] X. Wang, Y. Zhong, L. Zhang, Y. Xu, Spatial group sparsity regularized nonnegative matrix factorization for hyperspectral unmixing, *IEEE Transactions on Geoscience and Remote Sensing* 55 (11) (2017) 6287–6304. doi:10.1109/TGRS.2017.2724944.
- [47] D. Cai, X. He, J. Han, T. S. Huang, Graph regularized nonnegative matrix factorization for data representation, *IEEE Transactions on Pattern Analysis and Machine Intelligence* 33 (8) (2011) 1548–1560. doi:10.1109/TPAMI.2010.231.
- [48] D. C. Heinz, Chein-I-Chang, Fully constrained least squares linear spectral mixture analysis method for material quantification in hyperspectral imagery, *IEEE Transactions on Geoscience and Remote Sensing* 39 (3) (2001) 529–545. doi:10.1109/36.911111.
- [49] F. Geng, Z. Shi, Z. Jiang, J. Yin, Independent innovation analysis for hyperspectral imagery unmixing, in: 2008 Fourth International Conference on Natural Computation, Vol. 3, 2008, pp. 226–230. doi:10.1109/ICNC.2008.652.
- [50] D. Kitamura, N. Ono, H. Sawada, H. Kameoka, H. Saruwatari, Determined blind source separation unifying independent vector analysis and nonnegative matrix factorization, *IEEE Transactions on Audio, Speech, and Language Processing* 24 (9) (2016) 1622–1637.
- [51] D. Benachir, S. Hosseini, Y. Deville, M. S. Karoui, A. Hameurlain, Modified independent component analysis for initializing non-negative matrix factorization: An approach to hyperspectral image unmixing, in: 2013 IEEE 11th International Workshop of Electronics, Control, Measurement, Signals and their application to Mechatronics, 2013, pp. 1–6. doi:10.1109/ECMSM.2013.6648948.
- [52] D. Kitamura, N. Ono, H. Sawada, H. Kameoka, H. Saruwatari, Determined blind source separation unifying independent vector analysis and nonnegative matrix factorization, *IEEE/ACM Transactions on Audio, Speech, and Language Processing* 24 (9) (2016) 1626–1641. doi:10.1109/TASLP.2016.2577880.
- [53] E. M. M. B. Ekanayake, B. Rathnayake, E. M. H. E. B. Ekanayake, A. R. M. A. N. Rathnayake, H. M. V. R. Herath, G. M. R. I. Godaliyadda, M. P. B. Ekanayake, Enhanced hyperspectral unmixing via non-negative matrix factorization incorporating the end member independence, in: *IGARSS 2019 - 2019 IEEE International Geoscience and Remote Sensing Symposium*, 2019, pp. 2256–2259. doi:10.1109/IGARSS.2019.8899045.
- [54] L. Weixiang, Z. Nanning, Y. Qubo, Nonnegative matrix factorization and its applications in pattern recognition, *Chinese Science Bulletin* 51 (1) (2006) 7–18.

- [55] M. W. Berry, J. Kogan, Text mining : applications and theory (2010).
- [56] M. W. Berry, M. Browne, A. N. Langville, V. P. Pauca, R. J. Plemmons, Algorithms and applications for approximate nonnegative matrix factorization, *Computational Statistics & Data Analysis* 52 (1) (2007) 155–173.
- [57] Ye Zhang, Yong Fang, A nmf algorithm for blind separation of uncorrelated signals, in: 2007 International Conference on Wavelet Analysis and Pattern Recognition, Vol. 3, 2007, pp. 999–1003. doi:10.1109/ICWAPR.2007.4421577.
- [58] J. J. Burred, Detailed derivation of multiplicative update rules for nmf, 2017.
- [59] C. Boutsidis, E. Gallopoulos, Svd based initialization: A head start for nonnegative matrix factorization, *Pattern Recognition* 41 (4) (2008) 1350–1362. doi:https://doi.org/10.1016/j.patcog.2007.09.010. URL <http://www.sciencedirect.com/science/article/pii/S0031320307004359>
- [60] C. Shi, L. Wang, Linear spatial spectral mixture model, *IEEE Transactions on Geoscience and Remote Sensing* 54 (6) (2016) 3599–3611. doi:10.1109/TGRS.2016.2520399.
- [61] W. Wang, Y. Qian, Y. Y. Tang, Hypergraph-regularized sparse nmf for hyperspectral unmixing, *IEEE Journal of Selected Topics in Applied Earth Observations and Remote Sensing* 9 (2) (2016) 681–694. doi:10.1109/JSTARS.2015.2508448.
- [62] S. Jia, Y. Qian, Spectral and spatial complexity-based hyperspectral unmixing, *IEEE Transactions on Geoscience and Remote Sensing* 45 (12) (2007) 3867–3879. doi:10.1109/TGRS.2007.898443.
- [63] S. Jia, Y. Qian, Constrained nonnegative matrix factorization for hyperspectral unmixing, *IEEE Transactions on Geoscience and Remote Sensing* 47 (1) (2009) 161–173. doi:10.1109/TGRS.2008.2002882.
- [64] Chein-I Chang, Qian Du, Estimation of number of spectrally distinct signal sources in hyperspectral imagery, *IEEE Transactions on Geoscience and Remote Sensing* 42 (3) (2004) 608–619. doi:10.1109/TGRS.2003.819189.